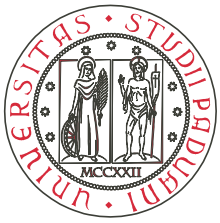

UNIVERSITÀ
DEGLI STUDI
DI PADOVA

Sede Amministrativa: Università degli Studi di Padova

Dipartimento di Ingegneria Idraulica, Marittima, Ambientale e Geotecnica

SCUOLA DI DOTTORATO DI RICERCA IN
SCIENZE DELL'INGEGNERIA CIVILE ED AMBIENTALE
CICLO XXIV

DIFFUSION OF FLOATING PARTICLES IN OPEN CHANNEL FLOW THROUGH EMERGENT VEGETATION

Direttore della Scuola: Prof. Stefano Lanzoni

Supervisore: Prof. Andrea Defina

Dottorando: Paolo Peruzzo

Abstract

In this thesis we study the problem of the dispersion of floating particles within emergent vegetation through experimental, numerical and theoretical analysis of the mechanisms that rule their temporary retention and the capture by plants.

In Chapter 1 we present early results of laboratory experiments performed to investigate the transport and the diffusion of floating particles (e.g., buoyant seeds) in open channel flow with emergent vegetation. The experiments are aimed at providing a better understanding of the relevant particle-vegetation interaction mechanisms responsible for the observed diffusion processes.

Qualitative observational data are then used to set up a stochastic model for floating particle transport and diffusion. Quantitative observations, such as the distribution of distances travelled by a particle before it is permanently captured by a plant (resembled *spartina maritima*) and the arrival time distributions at prescribed cross sections along the vegetated test section, are instead used to calibrate and validate the model. The comparison between theoretical predictions and experimental results is quite satisfactory and suggests that the observed relevant aspects of the particle-vegetation interaction processes are properly described in the model.

In Chapter 2 we present the results of a new laboratory investigation aimed at providing a better understanding of the transport and diffusion processes. The experiments are designed primarily to study the influence of vegetation density and flow velocity on the relevant interaction mechanisms between particles and vegetation. The aim is also to ascertain the validity of the stochastic model proposed in Chapter 1.

We find that *i*) the proper definition of plant spacing is given as $1/n_p d_p$, d_p being the plant diameter and n_p the number of plants per unit area; *ii*) the particle retention time distribution can be approximated by a weighted

combination of two exponential distributions; *iii*) flow velocity has a significant influence on the retention time and on the efficiency of the different trapping mechanisms, *iv*) vegetation pattern and density have a minor o negligible influence on the capture probability and on the retention time.

In the first part of Chapter 3 we study, in details, through a numerical model, the dynamics of capture due to surface tension (i.e. the Cheerios effect) of a cylindrical collector. The analysis shows that when capillary force is comparable to inertial forces the capture efficiency of the collector increases significantly with respect to the non-floating particle.

In the second part of Chapter 3, instead, we propose, and verify through laboratory experiments, some improvements to the model described in Chapter 1. In this case the emergent vegetation is simulated with an array of cylinders, randomly arranged, with the mean gap between cylinders far greater than the particle size, so to prevent the trapping of particles between pairs of cylinders, referred to as net trapping in Chapter 1. A good agreement is found also when comparing the model prediction with experimental data available in the literature for real seeds and more complex plant morphology.

Sommario

In questa tesi è stato studiato il problema della dispersione di particelle galleggianti in presenza di vegetazione emergente per mezzo di analisi sperimentali, numeriche e teoriche dei meccanismi che ne governano la ritenzione temporanea e la cattura da parte delle piante.

Nel Capitolo 1 sono presentati i risultati delle prove di laboratorio effettuate per indagare il trasporto e la diffusione di particelle galleggiati (ad esempio alcune varietà di semi) in un canale con vegetazione emergente. Questi esperimenti sono stati svolti per fornire una comprensione più ampia dei principali processi di interazione particella-pianta responsabili del processo diffussivo osservato.

Queste osservazioni qualitative sono state successivamente utilizzate per mettere a punto un modello stocastico per il trasporto e la diffusione di particelle galleggianti. Ulteriori dati raccolti sperimentalmente, quali la distribuzione delle distanze percorse dalle particelle prima di essere catturate permanentemente dalle piante e la distribuzione dei tempi di arrivo in alcune specifiche sezioni del tratto vegetato utilizzato nelle prove sperimentali, sono invece stati utilizzati per la calibrazione e la validazione del modello. Il confronto tra i risultati forniti dal modello e quelli sperimentali è soddisfacente e suggerisce che gli aspetti più rilevanti osservati nei processi di interazione particella-vegetazione sono opportunamente descritti dal modello.

Nel Capitolo 2 sono presentati i risultati di nuove prove sperimentali effettuate per approfondire la conoscenza dei processi di trasporto e di diffusione. In questo caso le prove sono state realizzate per valutare l'influenza della densità della vegetazione e della velocitá della corrente sui meccanismi di interazione precedentemente individuati. I risultati, infine, sono stati utilizzati per confermare la validitá del modello proposto nel Capitolo 1.

È stato trovato che *i*) la definizione più corretta di interasse tra le piante è $1/n_p d_p$, d_p, essendo d_p il diametro della pianta e n_p il numero di piante per

unità d'area, *ii*) la distribuzione dei tempi di ritenzione delle particelle può essere approssimato da una combinazione di due distribuzioni esponenziali opportunamente pesate, *iii*) la velocità della corrente ha un forte impatto sui tempi di ritenzione e sull'efficacia dei differenti meccanismi di cattura, mentre *iv*) la distribuzione e la densità della vegetazione gioca un ruolo di minor rilievo, se non addirittura trascurabile, sulla probabilità di cattura e sui tempi di ritenzione.

Nella prima parte del Capitolo 3 è studiata nel dettaglio la dinamica di cattura di un collettore cilindrico dovuta alla tensione superficiale (cioè l'effetto Cheerios). Lo studio mostra che, quando la forza capillare è comparabile alle forze inerziali, l'efficienza di cattura del collettore aumenta significamente rispetto al caso in cui le particelle siano non galleggianti.

Nella seconda parte del Capitolo 3, invece, sono proposte e verificate attraverso prove di laboratorio, alcune migliorie al modello introdotto nel Capitolo 1. In questo caso la vegetazione emergente è simulata da una schiera di cilindri, disposti casualmente, e distanziati tra loro in modo tale che le particelle non possano essere soggette alla cattura dovuta ad una coppia di cilindri e definita *net trapping* nel corso del Capitolo 1. Una buona corrispondenza è stata trovata anche quando i risultati forniti dal modello sono stati confrontati con alcuni dati sperimentali reperiti in letterattura relativi a semi reali ed a piante aventi una morfologia più complessa.

Acknowledgements

First and foremost I would like to express my sincere gratitude to my supervisor, Professor Andrea Defina, for his advices, teachings and for having always been supportive during my PhD; his competence and intuitions have been central in the outcome of this thesis.

I wish to acknowledge Simone Sponga, Daniele Destro, Pierfrancesco Da Ronco, Paolo Rachello and Fabrizio Benetton for their contribution to the experimental investigations.

My sincere thanks go to Professor Heidi Nepf for having given me the opportunity to spend seven months at Massachusetts Institute of Technology working in her lab, and for having been supportive and enthusiastic during our collaboration.

Finally my thanks go to Professor Roman Stocker: it was a pleasure and an honor for me to work with him in the last part of my research.

Contents

List of Figures

List of Tables

Introduction

Hydrochory, i.e. the transport of matter by water, is one of the most important processes on the maintenance, development and colonization of riparian community [e.g. *Nilson et al.*, 1994; *Anderson et al.*, 2000; *Rand*, 2000; *Merrit and Wohl*, 2002; *Riis and Sand-Jensen*, 2006).

In the hydrochory of riparian system propagules and seeds are distinguished in non-buoyant and buoyant. The behavior of non-buoyant seeds is similar to that of sediments or neutrally buoyant particles.

In this case experimental investigation performed both in situ and in the laboratory provided details of the diffusion processes in the presence of vegetation [*Lopez and Garcia*, 1998;*Nepf*, 1999; *White and Nepf*, 2003; *Loghtbody and Nepf*, 2006; *Sharpe and James*, 2006; *Murphy et al.*, 2007] and studied the main particle trapping mechanisms [*Palmer et al.*, 2004].

The vegetation affects the dispersion and deposition of particles indirectly by offering a resistance to the flow and entailing a decrease in the bed shear stress, and directly, trough the trapping of particles by leaves and stems. Buoyant and non-buoyant seed dispersal also occurs in tidal estuaries and coastal lagoons [e.g. *Huiskes et al.*, 1995; *Rand*, 2000; *Riis and Sand-Jensen*, 2006]. In fact, many salt-marsh species appear to be adapted to dispersal by water, as their diasporas such as seeds are able to float for some time in seawater [*Wolters et al.*, 2008]. The dynamics of salt-marsh are influenced by the hydrodynamics, i.e. by currents, tide and waves [*Callaghan at al.*, 2010, *Turner et al.*, 1999 and *Nilson et al.*, 2002] and, at the same

time, vegetation modifies the hydrodynamics within the canopy. A recent model to explain the dispersion within submerged vegetation under current-wave condition is provided by *Li and Yan* (2007) (see also *Li and Zhang*, 2010), while *Li and Yu* (2010) discuss the problem for the case of emergent vegetation.

Many studies demonstrate that waves increase significantly the dispersion of neutrally buoyant or suspended particles, [*Gaylord at al.*, 2002; *Jin and Ji*, 2005; *Patil et al.*, 2009; and *Sullivan and Williams*, 2010].

On the contrary, and although the floating seeds transport and trapping are important mechanisms to the survival and the springing up of the coastal plants [*Van der Heide et al.*, 2007; *Reise*, 2002; and *Bouma et al*, 2009], the literature is poor of examples in similar condition for floating particles.

Chang et al. (2008) provide data from field studies and laboratory experiments about trapping of buoyant seeds of several species of plants under different hydrodynamics conditions (i.e. tide, tide and flow, and tide, flow and waves). Through laboratory flume experiments the authors study the seed retention by applying three hydrodynamics treatments sequentially to the same seeds: *i*) flooding by filling the flume, *ii*) unidirectional flow and *iii*) wave action combined with unidirectional flow. In the experiments vegetation is initially emergent (during the flume filling) and subsequently is submerged. However any attempt understanding the mechanisms of retention due to the vegetation lacks.

Floating particles behave differently from suspended sediments because they are affected by further phenomena as wind drag or surface tension effects. Some studies show that the floating ability plays an important role to enhance aquatic seed dispersal [*Nilsson and Danvind*, 1997; *Van den Broek et al.*, 2005). Particularly *Van den Broek et al.* (2005) show that the long-floating ability of particles is possibly the main factor in order to disperse seeds for longer distances, while experiments in situ carried out by *Nilsson*

and Danvind (1997) show that no relationship is likely to exist between floating ability and the distribution of species along several Swedish rivers studied. This results highlight that other factors influencing the dispersion of floating particles can be important.

Merritt and Wohl (2002), through laboratory experiments, studied the effects of the hydrologic regime and channel morphology on seed deposition patterns in a laboratory channel with fluvial features such as flow expansions and constrictions, pools, point bars, islands, and slackwater areas. However, the complex channel morphology used in the experiments makes it difficult to identify the fundamental mechanisms responsible for the observed behaviors.

Chambert and James (2009) investigated the transport of 5 different buoyant seeds floating trough an array of vertical cylinders used to mimic an emergent plant canopy. The study showed that the trapping of seeds increased with increasing of stem density and with decreasing of particle mass. It was found that the main mechanism of capture was trough the Cheerios effect, whereby floating particles are attracted toward the cylinder by the rising meniscus. It was also observed that, unlike suspended sediment or neutrally buoyant tracer, floating particles were not often trapped in the wake region behind the cylinders. Moreover, the experiments show that wind proved more important to drift lighter seeds than the heavier ones.

All these studies give valuable insight into floating particle transport, diffusion, and trapping in the presence of emergent vegetation. However, they are not extensive enough to give a complete and detailed picture of the complex processes that govern floating particle dispersal, and there is a clear need for further research.

The aim of this thesis is to provide a comprehensive picture of the interactions mechanisms that rule the transport and diffusion process through experimental, numerical and theoretical analysis. Since the phenomena that affect the process of dispersion and capture of floating particles are manifold,

an exhaustive work that includes all these aspects is hardly feasible.

Some preliminary investigations in laboratory flume with plastic, partially emergent plants and in uniform flow conditions allowed us to recognize the main particle-plant interaction mechanisms that are responsible of mechanical longitudinal diffusion of floating particles in the riparian environments. Specifically, through video analysis of several particle trajectories, a slowdown of the particle motion was observed due to inertial impaction with the stems and wake trapping in the unsteady recirculation zone behind the plant. Other primary processes observed were the trapping by the Cheerios effect, i.e. effect of attraction between emergent bodies due to capillarity. In these cases particles were either slowed down or captured by leaves (temporary or permanently). Finally, because of the specific conformation of the vegetation used in the experiments (i.e. silicon plants resembling *SpartinaMaritima*), particles were also trapped by netlike structures formed by leaves. We named this trapping mechanisms net trapping.

Chapter 1

Floating particle trapping and diffusion

In this section we present early results of laboratory experiments performed to investigate the transport and diffusion of floating particles (e.g., buoyant seeds) in open channel flow with emergent vegetation. We use laboratory experiments to explore the details of the processes that control the interaction between floating particles and emergent vegetation.

The experiments are aimed at providing a better understanding of the relevant particle-vegetation interaction mechanisms responsible for the observed diffusion processes.

Qualitative observational data are then used to set up a stochastic model for floating particle transport and diffusion. Quantitative observations, such as the distribution of distances travelled by a particle before it is permanently captured by a plant and the arrival time distributions at prescribed cross sections along the vegetated test section, are instead used to calibrate and validate the model.

1.1 Experimental investigations

The experiments are carried out in a 6 m long, 0.3 m wide tilting flume. Water is recirculated through the channel via a constant head tank that maintains steady flow conditions. A magnetic flowmeter accurately measures the flow rate: a steady discharge of 2 l/s is introduced in the flume in all the experiments. Bed slope and a downstream weir are adjusted to achieve uniform flow conditions with a water depth of 0.1 ± 0.002 m resulting in a bulk velocity of 0.066 m/s (Fig. 1.1). The model plant canopy consists of plastic plants inserted into a 3.0 m long, perforated Plexiglas board which covers the middle part of the flume. The plastic plants, which resemble *SpartinaMaritima* (Fig. 1.2), are 0.15 m high and are comprised of approximately 120 leaves. Leaves have an elliptical section with the major diameter $d \approx 2$ mm and the ratio of minor to major axes of ≈ 0.7.

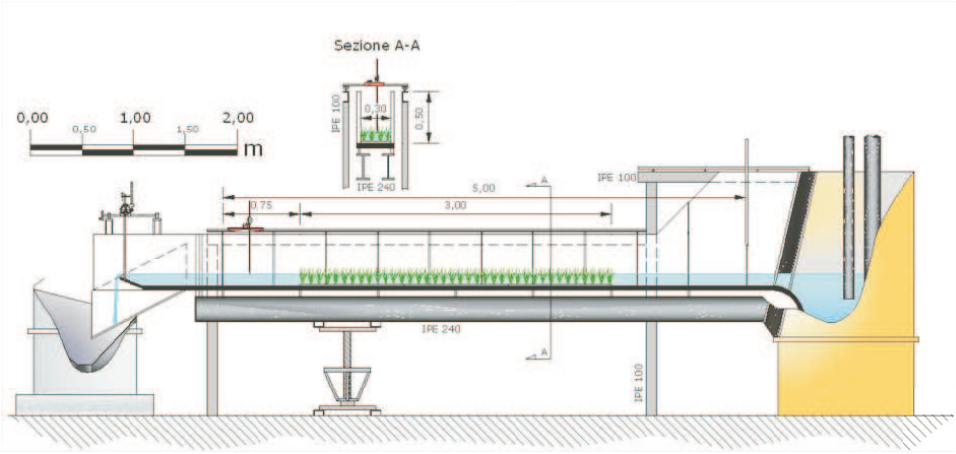

Figure 1.1: Scheme of the flume used in the experiments.

Two vegetation configurations are studied referred to as *staggered* and *random* in the text (see Fig. 1.3). The staggered configuration has a density $n_p = 87$ plants/m^2, the random configuration has a density $n_p = 56$ plants/m^2.

To achieve uniform flow across the test section bed slope is $s_b = 0.0034$

Figure 1.2: Plastic plant used in the experiments (left) compared to young *Spartina Maritima* collected in the lagoon of Venice (Italy) (right).

for the staggered configuration, and $s_b = 0.0025$ for the random configuration. Two different particles are used in the experiments to mimic buoyant seeds: particle A is an irregularly shaped wood particle which can be described approximately as a sphere having a diameter of 2.5 mm and a relative density of 0.95. Particle B is a smooth spherical berry with a diameter of 3.7 mm and a relative density of 0.83 (see Fig. 1.4).

Some preliminary investigations used lighter particles such as expanded Polystyrene (EPS) with a relative density of 0.03. However very light particles are extremely susceptible to trapping and all the particles released just upstream of the test section were permanently captured by the vegetation after traveling a short distance (shorter than 0.5 m for EPS particles). This behavior prevents us from performing a statistically reliable study of particle dispersal.

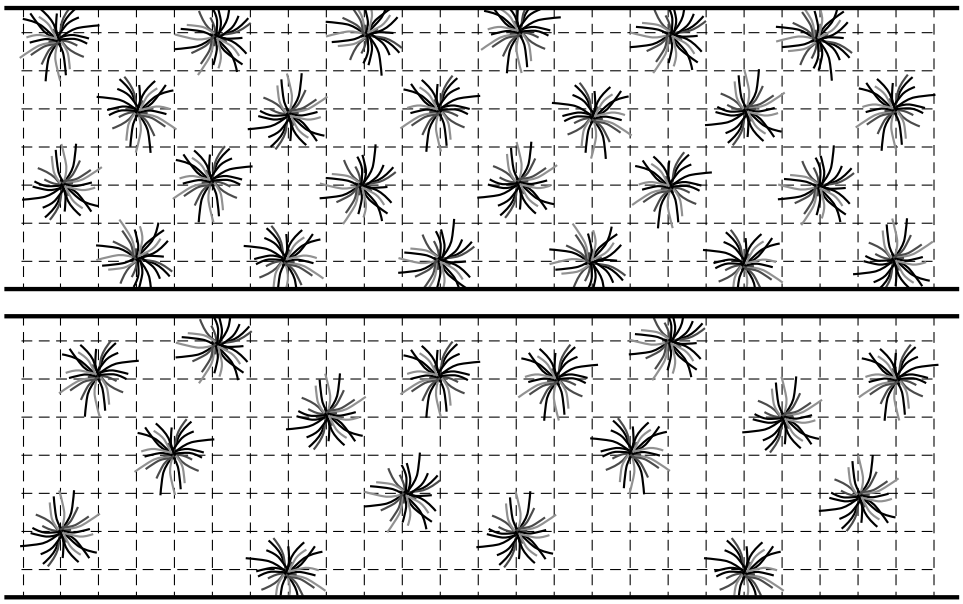

Figure 1.3: Vegetation configurations used in the experiments with notation. The upper panel shows the staggered configuration, the lower panel shows the random configuration. Spacing between *dots* on the flume bed is 4 cm; flow is from left to right.

In addition, we specify that this study focuses on longitudinal characteristics of floating particle dispersion, in fact the flume is relatively narrow and this does not allow for a meaningful study of the transverse diffusion. The relatively narrow channel width can also affect the longitudinal particle propagation, however, vegetation is likely to reduce the effects of lateral confinement by promoting a more uniform average velocity in the transverse direction.

Experimental observations are performed from both the Lagrangian and the Eulerian points of view.

Within the Lagrangian framework we release one single particle at a time just upstream of the test section and we observe the particle path and behavior. We also measure the distance travelled by the particle before it is permanently captured by a plant (we assume a particle is permanently

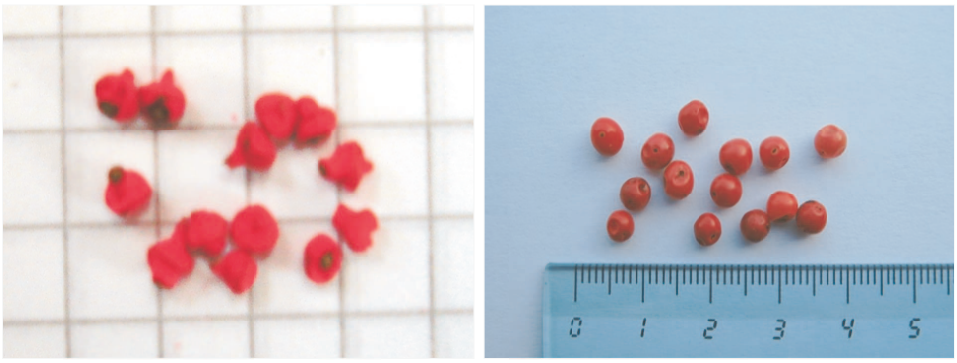

Figure 1.4: Particles used in the experiments: wood particles (particles A on the left, spherical berries (particles B) on the right.

captured if it stays attached to one plant for more than 10 minutes, i.e., a time interval that is longer by more than one order of magnitude than the mean time a particle takes to travel the whole test section).

For each vegetation configuration and particle type, approximately 400 particles are released and monitored to qualitatively observe the processes they experience and quantitatively evaluate the distance they travel before being permanently captured (see Table 1.1).

A few particle paths are also recorded with a camera mounted on a moving carriage, supported by a pair of rails along the flume, and driven by hand. Recorded frames (frame rate is 12.5 Hz) are then extracted and analyzed to track particle trajectory and to determine particle velocity. Accuracy in reconstructing instantaneous particle position is rather rough (particle position is determined with an error of $\pm$ 1 mm), however results give a reliable picture of particle path characteristics.

An example of the recorded particle trajectory is shown in Fig. 1.5 where we observe that the particle path is significantly affected by the heterogeneity of the velocity field induced by the vegetation. We observe eight interaction events, indicated with an arrow, where the particle is slowed down and its velocity reduces to zero for a very short time (less than 0.1 s). At x $\approx$ 0.25

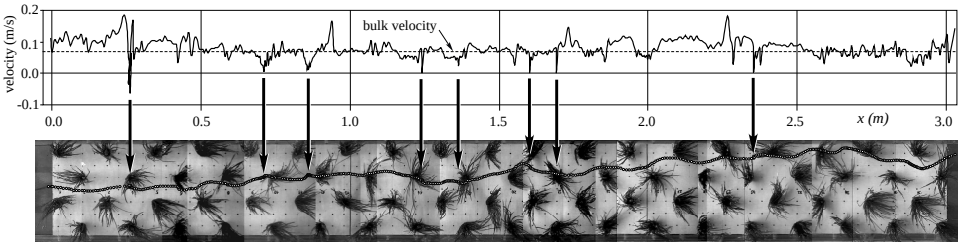

Figure 1.5: Particle longitudinal velocity as a function of the distance along the test section (upper panel), and plan view of the test section with the indication of the particle path (lower panel). Arrows denote the positions where particle-plant interaction occurs. Flow is from left to right.

m the particle enters the wake region behind a group of densely arranged leaves and it experiences an irregular motion with negative velocities; this wake trapping lasts approximately 1 s.

Fig. 1.6 shows the probability density function (*pdf*) of particle longitudinal velocity computed from the recorded particle trajectories: the *pdf* is biased toward the smaller velocities indicating that the diffusion process is controlled not only by temporal and spatial heterogeneity of the surface velocity field but also by the delay due to particle slowdown and/or short time trapping.

Within the Eulerian framework, groups of 50 particles are released at one moment uniformly distributed along a cross section just upstream of the test section and the passage of particles at fixed cross sections along the test section is recorded with a camera. Recording sections are located at the distances of 1.0 m, 2.0 m, and 3.0 m for particle A and 0.5 m, 1.0 m and 1.5 m for particle B from the upstream end of the test section. Eight groups with 50 particles are released for each vegetation configuration, particle type, and recording section. From the video analysis we determine the number of particles that pass the recording cross sections and we measure the time required by each particle to reach these sections (Fig. 1.7). It is worth noting, in Fig. 1.7, that scaling the distances X of the recording cross

sections by the length scale $1/\sqrt{n_p}$, n_p being the number of plants per unit area, makes the mean arrival times for particle A to collapse onto a single line regardless the vegetation configuration.

Direct observation and video analysis also allows us to recognize the relevant aspects of the interaction between floating particles and vegetation and the mechanisms responsible for the temporary and the permanent trapping of particles by plants.

When a particle interacts with a plant it is slowed down by three primary mechanisms: surface tension attraction through the Cheerios effect, inertial impaction, and wake trapping.

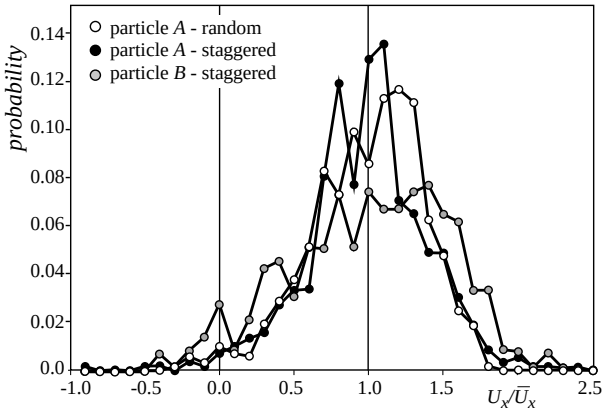

Figure 1.6: Probability density function of particle longitudinal velocity $U_x/\overline{U}_x$, $\overline{U}_x$ being the mean particle longitudinal velocity.

The Cheerios effect [e.g. *Vella and Mahadeven*, 2005] is the tendency for floating particles to be attracted towards a leaf by the rising meniscus: if a particle approaches a leaf within a distance comparable to the leaf diameter, then the particle is subject to an attracting force due to surface tension [*Chambert and James*, 2008].

We also observe inertial impaction [*Palmer et al.*, 2004] which occurs when a particle deviates from a streamline because of its inertia and collides with a leaf. However, because the particle size is comparable to the leaf

diameter, after the collision the particle goes around the leaf and, if its inertia overcomes the attractive force due to the Cheerios effect, it continues its way downstream. We specify that this mechanism can hardly be distinguished from surface tension attraction mechanism.

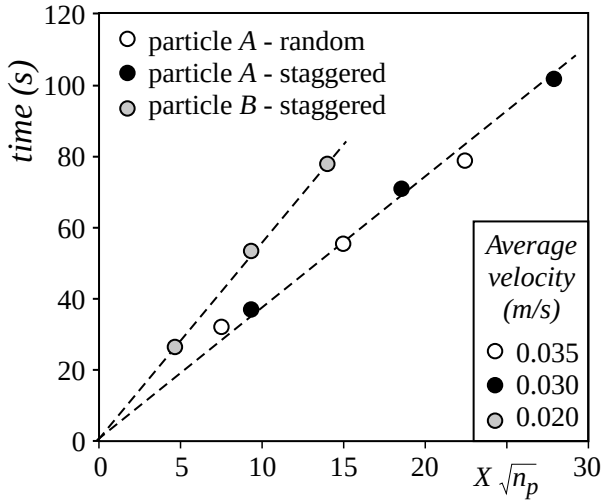

Figure 1.7: Mean time taken by particles to reach the fixed cross sections located at the non-dimensional distances $X\sqrt{n_p}$ from the upstream end of the test section.

Wake trapping [e.g., *White and Nepf*, 2003] is also observed: when a particle enters the unsteady recirculation zone behind a plant it follows an irregular path until it escapes or it is captured by a leaf through the Cheerios effect. However, in the present experiments very few particles are observed to enter the wake region behind a plant, which is consistent with the findings of *Merritt and Wohl* [2002].

It is to be specified that a plant is a porous obstacle to flow and the (weak) velocity defect region behind one plant is given as the superposition of all wakes forming behind each individual leaf of the plant; these wakes create a randomly heterogeneous velocity field that contributes to particle dispersion. More intense wake regions actually form behind groups of densely arranged leaves as in Fig. 1.5.

When a particle comes close to a leaf and the attractive force due to the

Cheerios effect overcomes particle inertia then the particle is captured and stays firmly attached to the leaf.

Particle capture also occurs when a few leaves of one plant (or, sometimes of two adjacent plants) weave each other to form a net-like structure which intercepts the floating particle. When a particle is captured through this mechanism, which is here referred to as net trapping, it remains finally trapped.

Sometimes, a trapped particle fastened to a single leaf through the Cheerios effect is observed to escape. The escaping occurs either when the particle is stricken by an energetic turbulent event (in this case we also observe a rapid shaking of the leaf) or, more frequently, when a particle is shaken off due to the quasi-periodic vibration of the leaf it is attached to.

In fact, we observe most of the leaves to vibrate at a frequency corresponding to that of vortex shedding. In the experiments the Reynolds number Re_d ($Re_d = Ud/\nu$, with d the diameter of a leaf, U the bulk flow velocity, and ν the kinematic viscosity) is in the range Re_d=120-150 (i.e., within the regular range from the beginning of the vortex shedding at $Re_d \simeq 47$ up to the transition of the wake at $Re_d \simeq 180$). In this range we have [e.g. *Fey et al.*, 1998]

$$Sr(Re_d) = 0.2684 - \frac{1.0356}{\sqrt{Re_d}} \tag{1.1}$$

where S_r is the Strouhal number ($S_r = fd/U$, with f the vortex shedding frequency). From Eq. 1.1 we have f = 5.2-6.9 Hz which well corresponds to the observed frequency at which leaves vibrate.

The amplitude of leaf oscillations we observe in the present experiments is approximately a_d = 2-3 mm; therefore the maximum transverse velocity of a particle attached to a leaf is $2\pi a_d f \approx 0.13$ m/s, which is greater than the mean flow velocity. Therefore, vibrating leaves might be capable of shaking off particles by overcoming the Cheerios effect.

We specify that this study considers low floating particle concentration. In fact, we observed that at moderately high particle concentration, the Cheerios effect promoted the formation of clusters comprised with a few particles. The clusters had a relatively smaller average velocity because of the more frequent interactions with the vegetation and were more easily captured by the vegetation as they get stuck against a group of few leaves.

In view of the mathematical model for floating particle trapping and diffusion described in the next section, we summarize the relevant, qualitative experimental observations as follows

- When a particle interacts with a plant (i.e., with one leaf or a few leaves) it can be either slowed down, or temporarily captured, or permanently captured.

- Mechanisms which slow down a particle are the Cheerios effect, inertial impaction, and wake trapping. Typical time delay in the particle propagation produced by this slowdown is about 2 s in the present experiments.

- If the attractive force, between a particle and a leaf, promoted by the Cheerios effect overcomes particle inertia, then the particle gets stuck to the leaf. However, the particle can escape thanks to the leaf vibration induced by the alternate vortex shedding. In the present experiments, this temporary trapping event produces a time delay in the particle propagation of some tens of seconds.

- When a particle is trapped through the net trapping mechanism or through the Cheerios effect by one leaf that cannot vibrate, the retention time is measured to be at least one order of magnitude greater than the previous one (i.e., more than 600 s in the present experiments). In this case we assume that the particle is permanently captured.

1.2 The stochastic model

We propose a stochastic model to simulate the transport and diffusion of floating particles and the trapping mechanisms observed in the experiments. The model is one-dimensional and describes particle-vegetation interactions along the curvilinear axis s corresponding to the generic particle trajectory. The place, along s, where a particle interacts with one leaf (or a few leaves) is here referred to as interaction point.

We dissect the particle path into segments Δs, Δs being the mean spacing between plants, and assume that the interaction points (one within each segment Δs) are arranged randomly in space with a uniform *pdf*.

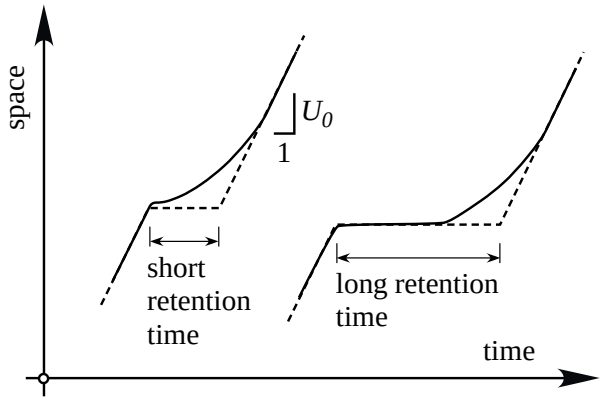

Figure 1.8: Actual (full line) and modeled (dashed line) world lines of a particle in the space-time diagram.

In the experiments we sometimes observe a particle interacting with two or more leaves of the same plant, wide apart each other, i.e., more than one interaction process with the same plant occurs. Here we assume that the slow-down process experienced by a particle interacting with more than one leaf of the same plant can be lumped into one single interaction event.

The proper specification of the length scale Δs is important to assess the model performance, as we will show. The mean centre-to-centre spacing between adjacent plants is $\Delta s_1 = 1/\sqrt{n_p}$, n_p being the number of plants per

unit area. The mean spacing along any straight line parallel to the direction of flow, is $\Delta s_2 = 1/n_p d_p$, d_p being the diameter of the plant [*White and Nepf*, 2003].

Based on comparison between model and experimental results we find that Δs_1 performs better than Δs_2; therefore the model assumes $\Delta s = 1/\sqrt{n_p}$.

Let P_i be the probability that a particle interacts with a plant (i.e., with a leaf or a group of leaves) while travelling the distance Δs along its path, transported by the flow (on average, a particle interacts with one plant over a path whose length is $\Delta s/P_i$).

Let P_c be the probability that a particle is permanently captured, if it interacts with a plant. Then, the probability that a particle travels a distance X greater than L before being finally captured is

$$P(X > L) = (1 - P_i P_c)^{n_L} \tag{1.2}$$

where n_L is the number of interaction points (i.e., plants) the particle meets within the distance L. We extend n_L to assume non-integer values and write $n_L = L/\Delta s$. Equation (1.2) is then rearranged to read

$$P(X > L) = e^{-L/\lambda} \tag{1.3}$$

where $\lambda = -\Delta s/ln(1 - P_i P_c)$ is the particle mean path length, while $1/\lambda$ is commonly referred to as retention coefficient [e.g., *Riis and Sand-Jensen*, 2006].

In the following we consider temporary trapping processes. We denote with t_0 the average time a particle spends to travel the distance Δs if no interactions with the vegetation occur. If a particle interacts with a plant and t is the time the particle actually spends to cover the distance Δs, then we define $\tau = t - t_0$ as the retention time and we assume that a particle travels within each segment Δs with velocity $U_0 = \Delta s/t_0$ and it is

temporarily arrested for the time τ (see Fig.1.8). Therefore, retention time, as presently defined, includes the delay due to the acceleration of a particle towards the velocity U_0.

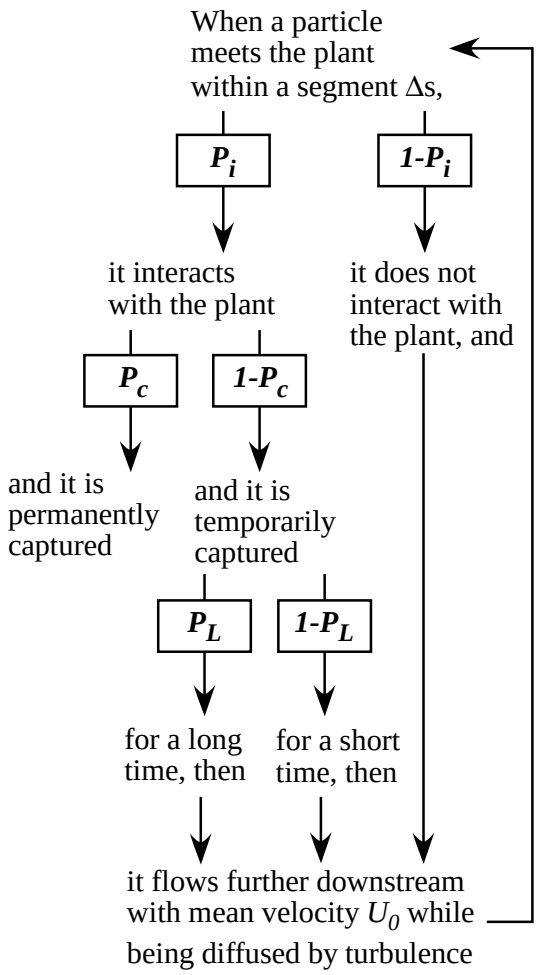

Figure 1.9: Schematic of the proposed model.

The velocity U_0 is slightly greater than the bulk velocity U both because the free surface velocity is greater than the depth average velocity and because of the channelling effect induced by plants.

When a particle interacts with the vegetation, within the generic Δs, it has the probability $1-P_c$ of being temporarily trapped. As stated at the end of Section 1.1, two different interaction mechanisms are mainly responsible

for particle propagation delay (i.e., particle slow down by the Cheerios effect, inertial impaction, and wake trapping, and temporary trapping events which occur when the attractive force due to the Cheerios effect overcomes particle inertia. Accordingly, we introduce a short (subscript S) and a long (subscript L) retention time and denote with P_S the probability that a particle is trapped for a short retention time (while $P_L = 1 - P_S$ is the probability that a particle is trapped for a long retention time).

The model further assumes that both short and long retention times are random and exponentially distributed with mean retention times T_S and T_L, respectively:

$$p_S(t) = \frac{1}{T_S} e^{-\frac{t}{T_S}} \tag{1.4}$$

$$p_L(t) = \frac{1}{T_L} e^{-\frac{t}{T_L}} \tag{1.5}$$

We specify that distinguishing long retention time trapping from permanent (i.e., infinite retention time) trapping is a reasonable modelling approximation. In fact, long and infinite retention times rely on two different trapping mechanisms. However, the issue is deserving of further investigation.

Floating particles are also subject to turbulent diffusion due to the temporal and spatial heterogeneity of the surface velocity field (e.g., *White and Nepf*, [2003]). This is included in the model; however, because the heterogeneity of the velocity field is moderately weak and the distance travelled by a particle before being definitely captured is relatively short, turbulent diffusion plays a minor role in affecting the dispersion pattern.

The overall model is schematically illustrated in Fig. 1.9. An analytical expression for the particle arrival time distribution function at prescribed cross sections is given in the Appendix A. However the analytical model is hard to handle and it does not account for the turbulent diffusion. For these

reasons we also set up a random walk particle-tracking model (see Appendix B), which we checked against the analytical solution. The theoretical results presented and discussed in the next section are obtained as the ensemble average of 10000 realizations computed with the random walk model.

1.3 Calibration of the stochastic model

Within the Lagrangian framework we measure the distance x travelled by each single particle, released just upstream of the test section, before it is permanently trapped by a plant: we can thus compare experiments with Eq. (1.3).

Figure 1.10 shows the probability a particle has of travelling a distance X greater than L for the three investigated cases: the experimental points actually follow an exponential law. This result, which largely corresponds with results from other studies [e.g., *Riis and Sand-Jensen*, 2006], is confirmed by the Eulerian measurements where we count the number of the released particles that reach and eventually pass some fixed cross sections downstream from the beginning of the test section (Fig. 1.10, square symbols).

Particle B is more susceptible to permanent trapping than particle A although both particles have approximately the same density and particle B, because of its greater size, has a much larger inertia. This is because, due to its size, particle B is more frequently captured through the net trapping mechanism. In fact, particle trapping through the net trapping mechanism occurs in 65% of cases for particle B and only in 45% of cases for particle A.

We determine the probability $P_i P_c$ for each of the three different experimental conditions (see Table 1.1) by fitting Eq. (1.3) to the experimental data.

For particle A the product $P_i P_c$ (or equivalently, the non-dimensional retention coefficient $\Delta s/\lambda$) remains approximately the same no matter the vegetation distribution and density. We speculate that, if a particle interacts with a plant then the probability P_c that this interaction will produce a permanent capture depends mainly on the particle and vegetation characteristics and on the flow velocity; on the contrary it is weakly affected by the vegetation distribution and density. Therefore, since $P_i P_c$ remains approximately the same for particle A, we conclude that the probability P_i of having an interaction does not depend on the vegetation distribution and density, as well.

This observation can be extended to the other model parameters which describe the local particle-vegetation interaction processes. Therefore, the parameters P_L, T_L, and T_S are expected to remain the same for the two vegetation configurations that use particle A. This idea is further supported by observing that even with a regular distribution of plants (i.e., the staggered configuration), from the point of view of a particle which is travelling along its path, interaction points appear to be randomly distributed with mean spacing Δs.

Within the Eulerian framework we also measure the time spent by particles to reach (and pass) some fixed cross sections and we use these data to construct the cumulative arrival time distributions. The experimental results are compared to the model predictions in Fig. 1.11. The values for the model parameters used in the computations and reported in Table 1.1 are determined through a trial-and-error calibration procedure.

In order to calibrate the model we preliminarily performed a sensitivity analysis to determine the effects of each single parameter on the arrival time distribution. We then calibrated the model through a trial-and-error procedure and checked the possibility of forcing model parameters to have the same value for different experimental configurations (e.g., values for P_L, T_L,

and T_S are the same for particle A and different vegetation configurations).

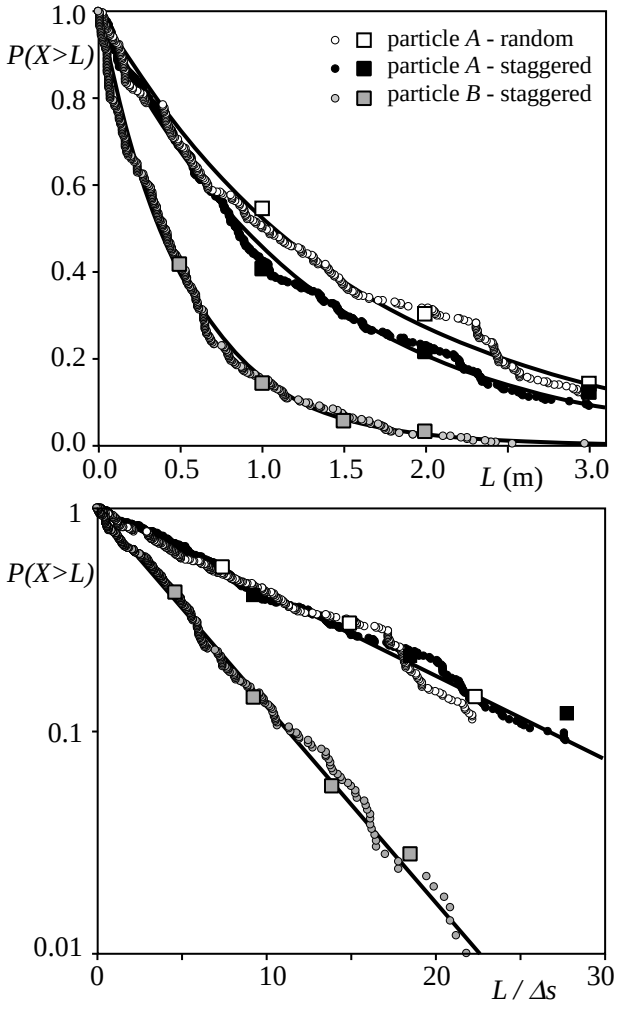

Figure 1.10: Experimental probability distribution $P(X > L)$ compared to Eq. 1.3. Probability is plotted versus L in the upper panel and versus $L/\Delta s$ in the lower panel. Circles and squares denote Lagrangian and Eulerian experimental results, respectively.

Model predictions compare favorably with experimental observations. The discrepancies shown in Fig. 1.11 can be mainly ascribed to the ir-

regular morphology of the plants (see Fig. 1.5). Indeed, the number of interactions experienced by each particle along its path is moderately small and the experimental paths cannot be safely regarded as realizations of a purely random process. Therefore, the experimental data used to determine the arrival time distributions are not statistically suitable enough to unambiguously serve as a basis for a definitive comparison with the model predictions.

Table 1.1: Summary of experimental results and model parameters calibration.

	Staggered particle A	Random particle A	Staggered particle B
$\Delta S\,(m)$	0.108	0.134	0.108
$\lambda\,(m)$	1.26	1.55	0.53
$\lambda/\Delta S$	11.7	11.5	4.9
$P_i P_c$	0.082	0.083	0.184
P_i	0.295	0.295	0.360
P_c	*0.278*	*0.281*	*0.511*
P_i/P_c	*1.06*	*1.05*	*0.704*
$P_i(1-P_c)$	*0.213*	*0.212*	*0.176*
P_L	0.105	0.105	0.105
$T_S\,(s)$	1.7	1.7	2.7
$T_L\,(s)$	55.0	55.0	80.0
$U_0\,(m/s)$	0.073	0.081	0.073

We observe an elbow in the curves plotted in Fig. 1.11 which reflects the two different (short and long) retention time distributions. For particle A, the two different vegetation configurations produce rather different arrival

time distributions (Fig. 1.11a, b). In particular, the elbow in the curves for the case of random distribution is significantly sharper than for the case of staggered distribution. Note that the model parameters P_i, P_c, P_L, T_S, and T_L are actually the same for both the vegetation distributions. This suggests that the observed different behaviors are solely (and effectively) controlled by the spacing Δs (i.e., the vegetation density) and that the choice of the length scale $\Delta s = 1/\sqrt{n_p}$ is reliable (see also Fig. 1.7). In addition this result confirms the idea that the model parameters depend on the local characteristics of the particle-vegetation interaction process and are unaffected or weakly affected by the vegetation distribution and density.

For the case of staggered configuration and particle A the mean number of interactions within the 3 m long test section is $3 \cdot P_i/\Delta s \approx 8$, which is consistent with the example shown in Fig. 1.5 where the arrows denote intense particle slowdowns.

Particle B, because of its greater inertia and size, is more susceptible to interact with the vegetation (it has a greater P_i) than particle A. However, the probability of being slowed down or temporarily captured (which is given by $P_i(1-P_c)$) is lower for particle B than for particle A. This behavior reflects the greater inertia of particle B which, accordingly, is less affected by the attractive force between a particle and a leaf promoted by the Cheerios effect.

Interestingly, the probability P_L is the same for both particles A and B. This suggests that the ratio between the number of slowdown events and temporarily trapping events might be independent from particle characteristics.

Short retention time for particle B is slightly greater than that for particle A. This again reflects the greater inertia of particle B which requires a longer time to regain the mean transport velocity once it is slowed down or arrested by one leaf.

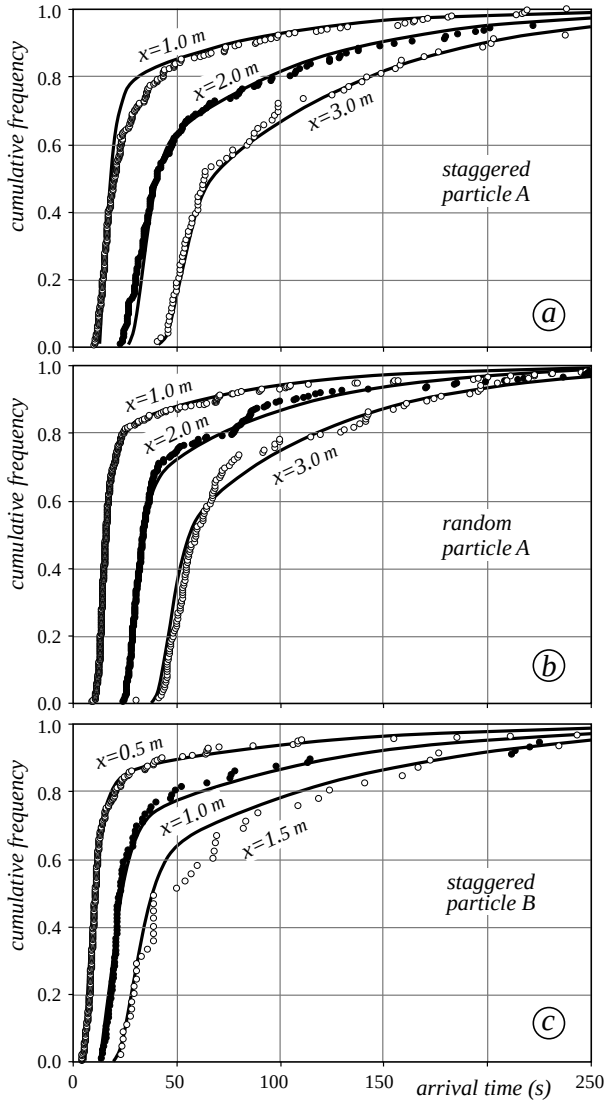

Figure 1.11: Cumulative arrival time distributions: comparison between experimental results (circles) and model predictions (full line).

The computed arrival time distributions plotted in Fig. 1.11 include turbulent diffusion due to the spatially non-uniform velocity field. The order of magnitude of the longitudinal diffusion coefficient D, is estimated on the basis of the few recorded particle trajectories. We consider only trajectory segments that do not include interaction events and compute D as $D = \sigma_U^2 \cdot \Delta t/2$, σ_U being the Standard Deviation of the longitudinal velocity and

$\Delta t = 0.08$ s is the inverse of the frame rate: we find $D \approx 2 \cdot 10^{-5}$ m^2/s. This is admittedly a very small diffusion coefficient which is however consistent with the small flow velocity (and Reynolds number) in the experiments.

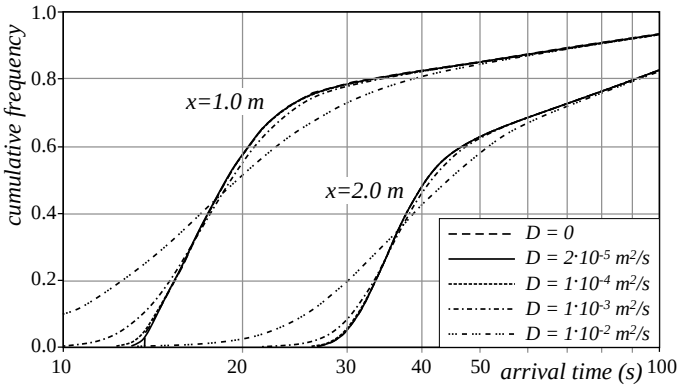

Figure 1.12: Cumulative arrival time distributions computed for different values of the diffusion coefficient. Model parameters used in the computations are those for particle A and staggered distribution of plants.

To assess the impact of turbulent diffusion we compute the arrival time distribution for different values of the diffusion coefficient. An example of these computations is shown in Fig. 1.12 where we see that increasing the diffusion coefficient by one or two orders of magnitude, turbulent diffusion has a minor impact on the solution. Note that the curves for $D = 0$, $D = 2 \cdot 10^{-5}$ m^2/s, and $D = 1 \cdot 10^{-4}$ m^2/s can hardly be distinguished. This result confirms that dispersion of floating particles in the presence of emergent vegetation is mainly related to particle-vegetation interaction processes.

Chapter 2

Additional experimental investigations: the effects of flow velocity and vegetation density

The stochastic model proposed in Chapter 1 distinguishes three different effects on the particles motion due to vegetation: *i*) a short delay in the propagation due to the slow down and short time trapping (i.e. temporary trapping for a short retention time), *ii*) a long delay due to retention by the leaves through the Cheerios effect or by weak net trapping (i.e. temporary trapping for along retention time) and *iii*) permanent captures (particle retention lasts longer than the time scale of the experiments) due to the Cheerios effect and through the net trapping (see fig. 2.1).

In the model the interaction frequency and the kind of the processes are weighted through three simple probabilities: the probability of interaction P_i, the probability of capture P_c and the probability of being trapped for a long retention time P_L. All these parameters were not measured in the pre-

vious experiments. They were determined through a calibration procedure performed to fit the measured arrival time distributions.

The goal of the experimental study described in this chapter is to study more in depth the details of the main processes that affect particle diffusion and trapping. Investigations are focused on the quantitative analysis of the basic factors that affect the mechanisms of interaction. Specifically, laboratory investigations are aimed at evaluating the effects of vegetation density and pattern and of flow velocity.

Figure 2.1: trapping of floating berries (particles B) by emergent vegetation: examples of net trapping capture and capture by the Cheerios effect.

2.1 Further experimental investigation

As stated above, we use laboratory experiments to explore the details of the processes that control floating particle transport and diffusion in the presence of emergent vegetation. Observational data are then used not only to strengthen and advance our knowledge, but also to validate and improve the stochastic model described in Chapter 1, which is likely to include all the relevant aspects of floating particle-vegetation interaction processes. In particular, we focus on the basic interaction mechanisms between floating particles and vegetation stems and leaves (i.e., inertial impaction, wake and net trapping, and trapping due to the Cheerios effect) which affect particle propagation by promoting propagation delay, permanent captures and diffusion. We also focus on the impact of flow velocity and of vegetation pattern and density on the efficiency of these mechanisms.

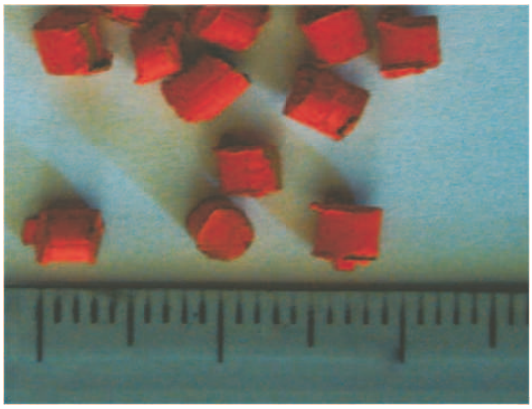

Figure 2.2: Wood cylinders used in the experiments (particles C).

The experiments are carried out using the same flume and plants described in Section 1.1. To mimic buoyant seeds, in this case, we used small wood cylinders having equal diameter and height of 3 mm and a relative density of ≈ 0.7 (see Fig. 2.2).

Particles are released all along a cross section approximately 10 cm upstream the vegetated reach. Particles are allowed to dry before being re-

leased into the flow and they are released one at a time to avoid the formation of clusters. Indeed, we assume that a particle is permanently captured if retention time is greater than 600 s, consistently with the previous experiments.

For each vegetation density and bulk flow velocity approximately 400 particles are individually released and monitored. Most of particle runs are recorded with a camera (frame rate is 12.5 Hz) mounted on a moving carriage, supported by a pair of rails along the flume and driven by hand. Recorded frames are then extracted and analyzed to track particle trajectory, to determine particle velocity, and to measure the duration of temporary trapping events (see Table 2.1). Accuracy in reconstructing instantaneous particle position is sufficiently good (particle position is determined with an error of $\pm$ 1 mm), and results give a reliable picture of particle path characteristics. The distance travelled by each particle before being permanently captured is also measured. Direct observation and video analysis also allows us to recognize the relevant aspects of the interaction between floating particles and vegetation and the mechanisms responsible for the temporary and the permanent trapping of particles by plants.

Two sets of experiments are performed (see Table 2.1). Set A is designed to explore the impact of vegetation density on the type and frequency of the different interaction mechanisms. In set B we study the impact of flow velocity on the characteristics of the diffusion process. With data of set B we also explore the adequacy of some model assumptions such as the statistical distribution of residence time.

2.2 Evaluation of vegetation spacing

The proper specification of the (global) length scale Δs is important to assess the model performance. In fact, as argued in Section 1.3, most of model parameters turn out to be independent from vegetation pattern and

Table 2.1: Summary of experimental conditions and measured parameters for the two sets of experiments. Each set is composed of a group of experiments with a unifying physics: in set A flow velocity is held constant and vegetation density varies in the range 20 to 86.7 plants/m^2; in set B flow velocity is varied between 0.033 and 0.167 m/s and vegetation density is held constant. X denotes measured data.

Exp. set	Experiments	U (m/s)	n_p (m^{-2})	Video recording	number of runs	$P(X > L)$	Retention time	Trajectories	Arrival time
	A1		20.00		450	X			
	A2		27.78		400	X			
	A3		36.67		400	X			X
A	A4	0.033	46.67		400	X			
	A5		55.56	X[a]	400	X		X	
	A6		70.00		400	X			
	A7		86.67		400	X		X	
	B1	0.033		X	400	X	X	X	X
	B2	0.050		X	340	X	X	X	X
	B3	0.067		X[a]	434	X	X[b]	X	X
B	B4	0.083	86.67		400	X			
	B5	0.100			400	X			
	B6	0.133		X	424	X	X	X	X
	B7	0.167			400	X			

a) only a few runs are video-recorded in order to track particle trajectory

b) measured by a stopwatch

Figure 2.3: Overall view of the flume with plastic plants used in the experiments: $n_p = 55.6$ plants/m^2, random pattern.

density by normalizing lengths to the proper length scale.

The problem has two intrinsic length scales; these are the diameter of the bush, d_p and the mean centre-to-centre spacing between adjacent plants $1/\sqrt{n_p}$, n_p being the number of plants per unit area. Other length scales such as the leaf diameter d or the size of the recirculation zone behind leaves are mainly related to turbulent diffusion [*White and Nepf*, 2003]. Through an analysis of the particle velocity obtained from the reconstructed trajectories, we find that turbulent diffusion coefficient lies in the range between 10^{-5} and $2 \cdot 10^{-4}$ m^2/s. Since in Section 1.3 it was shown that turbulent diffusion negligibly contributes to the overall diffusion process, then these length scales are not considered in the present analysis.

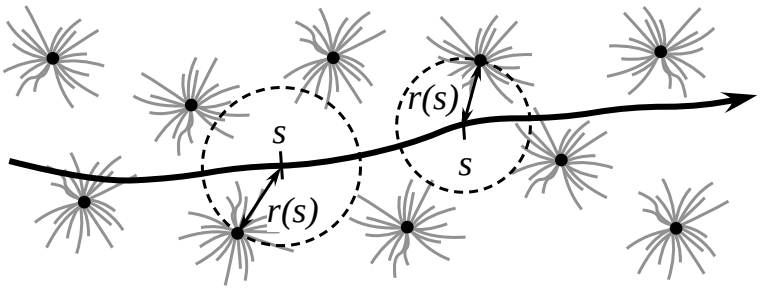

Figure 2.4: Schematic of a particle trajectory with notation defining $r(s)$.

In Chapter 1 we argued that the most appropriate length scale is the spacing $\Delta s = 1/\sqrt{n_p}$. However, this guess was based only on two sets of data with a moderately different vegetation density (i.e., $n_p = 85$ plants/m^2 and n_p=56 plants/m^2). In order to ascertain the most significant length scale we perform suitable experiments (set A in Table 2.1) in which only vegetation density is changed.

In these experiments we reconstruct and analyze some particle trajectories in order to see if and how they are affected by the presence of the plants. To analyze particle trajectory, we introduce the function $r(s)$ which measures the distance from a point along the trajectory to the nearest vegetation center as shown in Fig. 2.4, and we define the mean distance r_m as

$$r_m = \frac{1}{X} \int_X r(s) ds \tag{2.1}$$

where X is the path length.

We then introduce the distance R as the average of r_m computed over an infinite number of paths and define R_0 to be the distance R when paths are straight lines. Interestingly, the same value R_0 is found if paths are not straight lines but they are random. Accordingly, if paths are not affected by the presence of plants, i.e., they are random, then their mean distance R should be close to R_0. In case of staggered plants disposition, if a particle

follows a path zigzagging its way through the plants as shown in the right-lower corner of Fig. 2.5 (e.g., due to channelling effect) then a value for R greater than R_0 is found. Contrarily, if a particle path joins the centers of adjacent plants as shown in the left-upper corner of Fig. 2.5 then a value for R smaller than R_0 is found. We can then assume that the ratio R/R_0 measures the randomness of a particle path. The analysis can be extended to random plants disposition. In this case the limit values of R in Fig. 2.5 are average values.

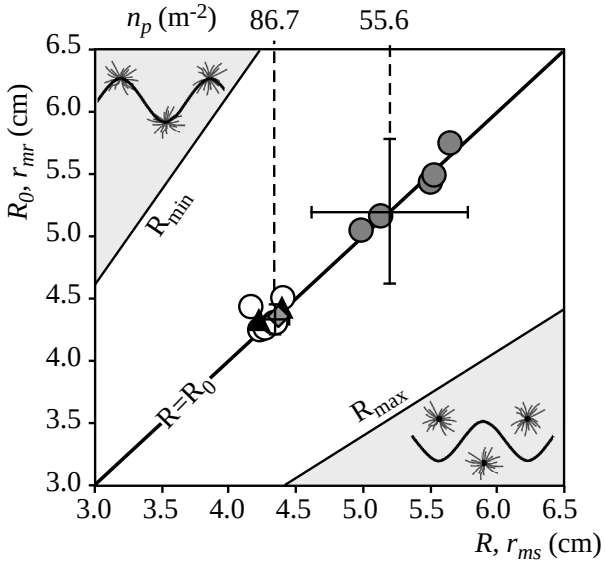

Figure 2.5: Plot of r_{mr} (and R_0) versus r_{ms} (and R). Points along the line of perfect agreement indicates that the path is random. The theoretical values of $R = R_0$ for $n_p = 86.7$ plants/m^2 and $n_p = 55.6$ plants/m^2 are indicated: the bar length represents one standard deviation (σ_{R_0}). R_{max} is the value of R when plants are arranged in a staggered pattern and particle trajectory is that shown in the right-lower corner; R_{min} is the value of R when particle trajectory is that shown in the left-upper corner. Open circles denote (r_{ms}, r_{mr}) points for $n_p = 86.7$ plants/m^2 (present experiments). The plot also includes the results of experiments performed in Chapter 1 with different particle types: particle A, $n_p = 55.6$ plants/m^2 (gray circles), particle A, $n_p = 86.7$ plants/m^2 (gray diamond), particle B, $n_p = 86.7$ plants/m^2 (black triangles).

Since we have a small number of measured paths, a less rigorous procedure is adopted to ascertain whether or not vegetation controls particle trajectory. For each measured path we compute the mean distance r_m (r_{ms}). We then fit the measured path to a straight line and compute the mean distance of plants from this line (r_{mr}). Fig. 2.5 shows the computed points (r_{ms}, r_{mr}) for different vegetation pattern and density and different flow velocity. Since all points cluster about the line $R = R_0$ with a small scatter compared to the theoretical standard deviation we argue that particle paths are random and weakly controlled by plants. This behavior is possibly due to the high porosity that characterize the plants used in the experiments. Plant porosity, here defined as $1 - n_L d^2/d_p^2 \approx 0.95$ (with n_L the number of leaves of one plant), is in fact large and comparable to the overall canopy porosity given as $1 - n_L(\pi d^2/4)n_p = 0.97 \sim 0.99$. In addition, random distribution of interaction points (i.e., points where leaves pierce the free surface) is likely to prevent the formation of preferential flow paths and the occurrence of channeling effect.

For a straight path (or, equivalently, for a random path) the mean spacing is given by $\Delta s = 1/n_p d_p$ [*White and Nepf*, 2003]. Therefore, we can safely assume that this spacing is the proper length scale, at least when vegetation is highly porous.

Some ambiguity however arises in defining the spacing this way since the plant diameter cannot be precisely defined or easily determined. However, as we show below, possible small errors in estimating d_p can be compensated by suitable tuning of the interaction probability P_i.

In this series of experiments (set A in Table 2.1), in which only vegetation density is changed, we also measure the distance X travelled by particles before permanent capture, whose distribution is given by eq. 1.3.

By fitting experimental data to Eq. 1.3 we determine the mean path length which is plotted against vegetation density in Fig. 2.6. The results

suggest that mean path length goes as the inverse of vegetation density (full line in Fig. 2.6).

It is interesting to observe that, when the probability P_c is moderately small, the mean path length can be approximated as

$$\lambda = -\frac{\Delta s}{\ln(1 - P_i P_c)} \approx -\frac{\Delta s}{P_i} \frac{1}{\ln(1 - P_c)} \tag{2.2}$$

Moreover, we can safely assume that the probability P_c depends on local factors (i.e., on particle and vegetation characteristics, and flow velocity) and it is weakly affected by the vegetation pattern and density. Accordingly, and from Eq. 2.2, the ratio $\Delta s/P_i$, which is the mean spacing between two successive interactions, has the same trend as that of λ. Since both λ and Δs go with the inverse of n_p we argue that the probability P_i is likely to be independent of vegetation pattern and density, in agreement with the results find in the previous experiments (see Section 1.3).

It is worth noting that any error in evaluating Δs (e.g., because of an incorrect evaluation of the plant diameter) can be compensated through the tuning of P_i.

2.3 Retention time distribution as function of velocity flow

In the stochastic model describe in Section 1.2 the retention time is assumed distributed according to the sum of two exponential distributions (eq. 1.4 and eq. 1.5) weighted by the probability P_L that a particle experiences a long retention time event

$$P(T > t) = P_L e^{-t/T_L} + (1 - P_L) e^{-t/T_S} \tag{2.3}$$

where T_S and T_L are the short and long mean retention time, respectively. The reason for assuming two different time scales stems from the different

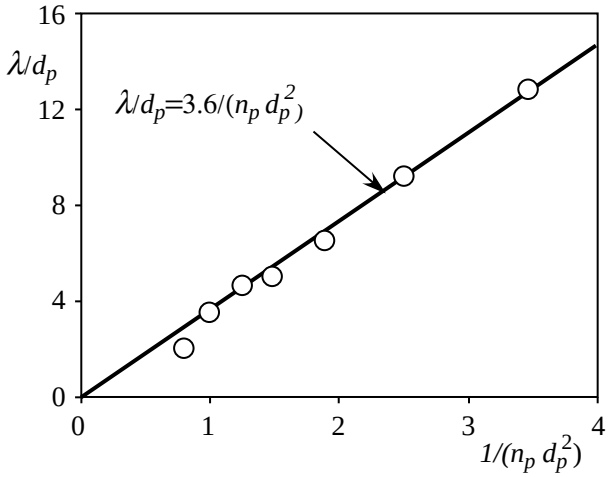

Figure 2.6: Mean path length as a function of vegetation density (set A). Distance *lambda* and vegetation density n_p are normalized by the plant diameter d_p. Since $1/n_p d_p$ is the mean spacing between two plants, a particle travels on average a distance of 3.6 times the mean plant spacing before a permanent capture occurs.

interaction mechanisms responsible for particle propagation delay observed in the experiments. The reliability of the assumption was indirectly verified through the comparison of measured and modelled arrival time distribution. However, retention time distribution was not directly measured.

In this work we use video-recorded paths of experimental set B to quantitatively evaluate retention times. Frame by frame analysis of the recorded paths allows us to measure the time that each particle spends at rest because of a temporary trapping event.

The cumulative probability $P(T > t)$ is then estimated on the basis of the relative cumulative frequency as

$$P(T > t) = 1 - \frac{i + N_0}{N_i + N_0 + 1} \tag{2.4}$$

where i is the number of measured data T with a value smaller than the reference value t, N_i is the total number of measured data, and N_0 is the guessed number of temporary trapping events that, for being too short, cannot be measured. In fact, we cannot accurately measure retention times

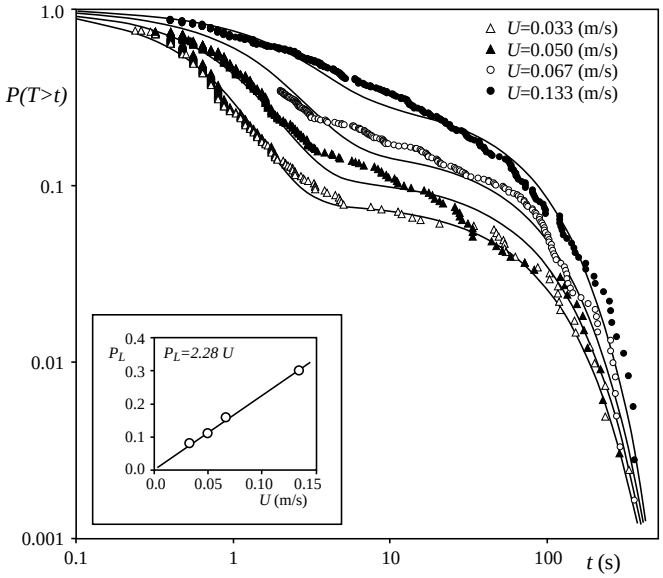

Figure 2.7: Experimental probability distribution $P(T > t)$ (symbols) compared to Eq. 2.3 (full lines). The inset shows the linear relationship between bulk flow velocity and the probability P_L)

shorter than about 0.25 s, the frame rate being 12.5 s^{-1}.

Parameters T_L, T_S, P_L, and N_0 are then determined by fitting measured retention times to Eq. 2.3 according to the procedure outlined in Appendix C (see Table 2.2).

The results are plotted in Fig. 2.7 which also includes the data measured with a stopwatch while visually observing travelling particle behavior. In this case, retention times shorter than 2 s were not considered in the analysis because, due to the measuring technique, they are likely affected by large uncertainty. Since shorter retention time events are lacking in this case, the chosen value for N_0 is rather uncertain due to the long extrapolation involved.

The experimental data are fitted reasonably well by Eq. 2.3. We also explore the possibility of using different probability distribution functions to fit the measured data. For example, we find that the Weibull distribution

Table 2.2: Summary of experimental conditions and results for video recorded experiments of set B.

U (m/s)	0.033	0.050	0.067	0.133
N_i	308	247	209	313
N_0	98	82	400	47
N_c	400	340	420	365
N_{ip}	1022	1175	–	6849
$T_L(s)$	90	88	85	80
$T_S(s)$	0.7	1.0	1.6	2.4
P_L	0.08	0.11	0.16	0.30
$T_{rest}(s)$	7.8	10.6	14.9	25.7

performs very well when bulk flow velocity is large (e.g., U=0.133 m/s) however, it largely fails in fitting slow flow data.

It is worth noting that mean retention time T_{rest} increases with increasing bulk flow velocity (see Table 2.2). This experimental result is rather surprising and far from being intuitive since one would expect the opposite. In fact, interaction mechanisms like the net trapping and the Cheerios effect do not depend on flow velocity whereas particle inertia increases with flow velocity. A possible explanation of this behavior is that at slow flow velocity only weak and short-lasting interaction events produce a temporary trapping, whereas stronger interactions produce permanent capture (i.e., events which are not considered in the analysis of retention time distribution). This is the reason why the probability P_L decreases with decreasing flow velocity.

The behavior is also consistent with the proposed model in which the probability P_i filters out all "interaction events" characterized by a retention

time so short that it can be regarded as zero. In fact, at each interaction point, particles have the probability 1-P_i of experiencing a trapping event characterized by a negligibly short retention time. The proposed model is thus formally equivalent to a model in which particles actually interact with vegetation at each interaction point and the retention time distribution is given as

$$P(T > t) = \begin{cases} 1 & t = 0 \\ P_i \left[P_L e^{-t/T_L} + (1 - P_L) e^{-t/T_S} \right] & t > 0 \end{cases} \tag{2.5}$$

Eq.2.5 suggests that the overall retention time (i.e., the total time a particle spends at rest during one run) decreases with increasing flow velocity provided that the probability P_i decreases rapidly enough with increasing flow velocity.

Table 2.3: Summary of experimental conditions and results for experiments of set B.

U (m/s)	0.033	0.050	0.067	0.083	0.100	0.133	0.167
λ (m)	0.19	0.28	0.69	0.88	1.11	1.79	1.98
$P_i P_c$	0.394	0.287	0.130	0.103	0.083	0.052	0.047
P_i	0.798	0.569	0.32[a]	–	–	0.106	–
P_c	0.499	0.504	–	–	–	0.494	–
U_0 (m/s)	0.046	0.060	0.072	–	–	0.133	–

a) extrapolated from Fig. 2.8

We use experimental data of set B to estimate how P_i and P_c, separately,

vary with flow velocity. Using the measured path length X_i of the i-th experimental run we compute the total number of interaction points N_{ip} as

$$N_{ip} = \sum_{i=1}^{N_{runs}} int(1 + X_i/\Delta s) \tag{2.6}$$

where $int()$ denotes the integer part of a real number and N_{runs} is the number of runs (see Table 2.1). Given the number of permanent captures (N_c) and the number of measured (N_i) and guessed (N_0) temporary interaction events (see Table 2.2), the probability P_i is estimated to be

$$P_i = (N_0 + N_i + N_c)/N_{ip} \tag{2.7}$$

The probability P_c is then computed from P_iP_c. The behaviors of probabilities P_iP_c, P_i, and P_c as a function of bulk flow velocity, as well as that of λ are plotted in Fig. 2.8; the numerical values are given in Table 2.3.

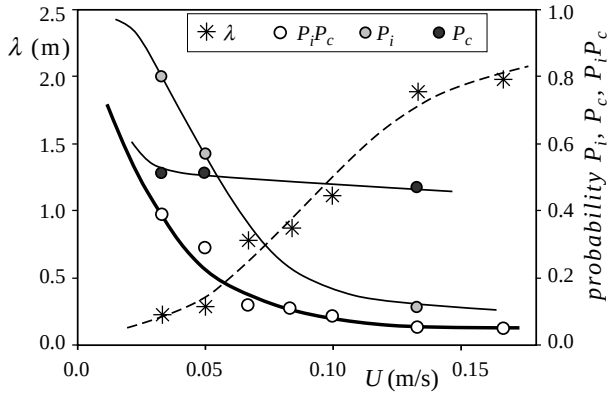

Figure 2.8: Mean path length and probabilities P_i, P_c, and P_iP_c as a function of bulk flow velocity.

Fig. 2.8 shows that the probability P_i actually decreases with increasing flow velocity. We speculate that, when flow velocity is (relatively) high then the Cheerios effect, alone or in combination with inertial impaction or wake trapping, is not able to determine a "significant" interaction event. Accordingly, the distance $\Delta s/P_i$ between two successive interactions increases with

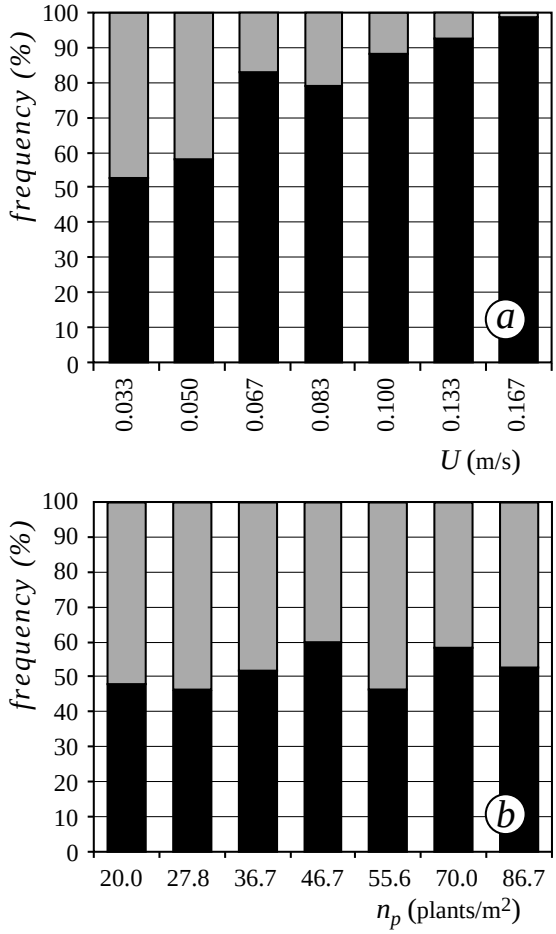

Figure 2.9: Efficiency of the observed permanent capture mechanisms as a function of *a*) flow velocity (n_p = 86.67 plants/m^2) and *b*) vegetation density (U = 0.033 m/s). The net trapping (*black*), and the Cheerios effect (*grey*).

increasing velocity. On the contrary, permanent trapping events which are mainly due to the net trapping mechanism, is moderately affected by flow velocity and the probability P_c remains fairly constant. However, at very low flow velocity, the Cheerios effect is sufficient to overcome friction drag and particle inertia, and both P_i and P_c are expected to approach unity as U goes to zero (Fig. 2.8).

Inspection of recorded paths, as well as visual observation, allows us to evaluate the frequency of occurrence of the different mechanisms responsi-

ble for permanent capture events, at different flow velocity and vegetation density. Fig. 2.9a shows that the Cheerios effect is effective only at slow flow velocity whereas the net trapping mechanism, enhanced by the Cheerios effect, is by far the most frequent permanent capture mechanism also at moderately slow flow velocity. We also observe that, at slow flow velocity, a small fraction of permanent captures ($\approx 5\%$) occurs because particles get stuck to the channel wall through the Cheerios effect. In fact, near the wall the velocity is very small and the drag force is not sufficient to re-entrain particles into the main flow. These events are not included in the present analysis. Fig. 2.9b compares the efficiency of the different permanent capture mechanisms at different vegetation densities. No evident trend can be observed further confirming that particle-vegetation interaction process is a local one, marginally affected by vegetation pattern and density.

For each particle run we also compute the mean particle velocity $u_X = X/t_X$, t_X being the time required for a particle to travel the whole path length, X. The mean particle velocity is distributed according to a bimodal probability density function (Fig. 2.10) thus reinforcing the idea that the diffusion process is governed by two, dramatically different time scales. Note that the number of temporary trapping events $\approx \lambda P_i/\Delta s - 1$ is, on average, less than two in the present experiments. Moreover, since $P_S = 1 - P_L = 0.7 \sim 0.9$, most of the events are short time captures, whereas in the few remaining events particles experience (at least) one long time trapping event, characterized by a mean retention time $T_L = 70 \sim 90$ s which is much longer than the time a particle takes to travel its trajectory when only short time trapping events occur. This is the reason why the mean particle velocity u_X is extremely slow when one (or, less frequently, more than one) long time interaction event occurs, whereas in the absence of long retention time events the mean velocity u_X is just smaller than the bulk flow velocity.

Fig. 2.10 also shows that the second peak is skewed to the left indicating

that the diffusion process is not Gaussian even excluding long time trapping events.

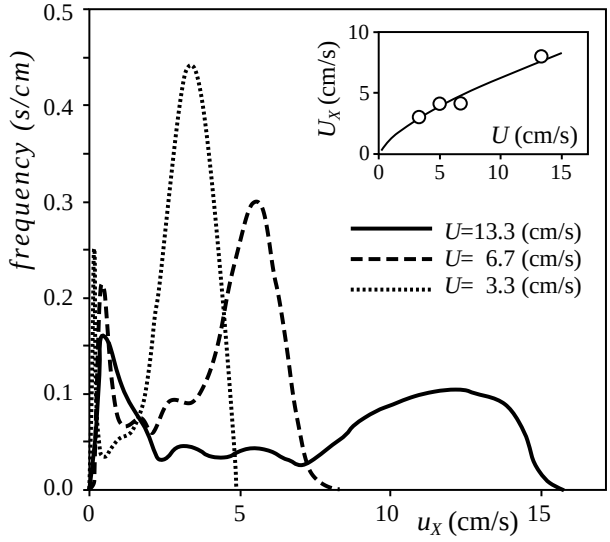

Figure 2.10: Probability density function of mean particle velocity u_X for $n_p = 86.7$ plants/m^2 and different bulk flow velocities. Inset: plot of average mean particle velocity, U_X versus bulk flow velocity, U.

2.4 Arrival time distribution

Using video-recorded paths (experiments A3 and experiments of set B), we also determine the time T_a spent by particles to reach some fixed cross sections and we use these data to construct the cumulative arrival time distributions. The experimental results are compared to the model predictions in Fig. 2.11.

Importantly, the values for the model parameters are not determined through a calibration procedure. In fact, probability P_L, and mean retention times T_S and T_L, whose values are given in Table 2.2, are determined through a best-fitting regression procedure on the measured retention times; probabilities P_i and P_c have been determined as discussed in the previous

sections (see Eq. 2.7 and Eq. 2.2).

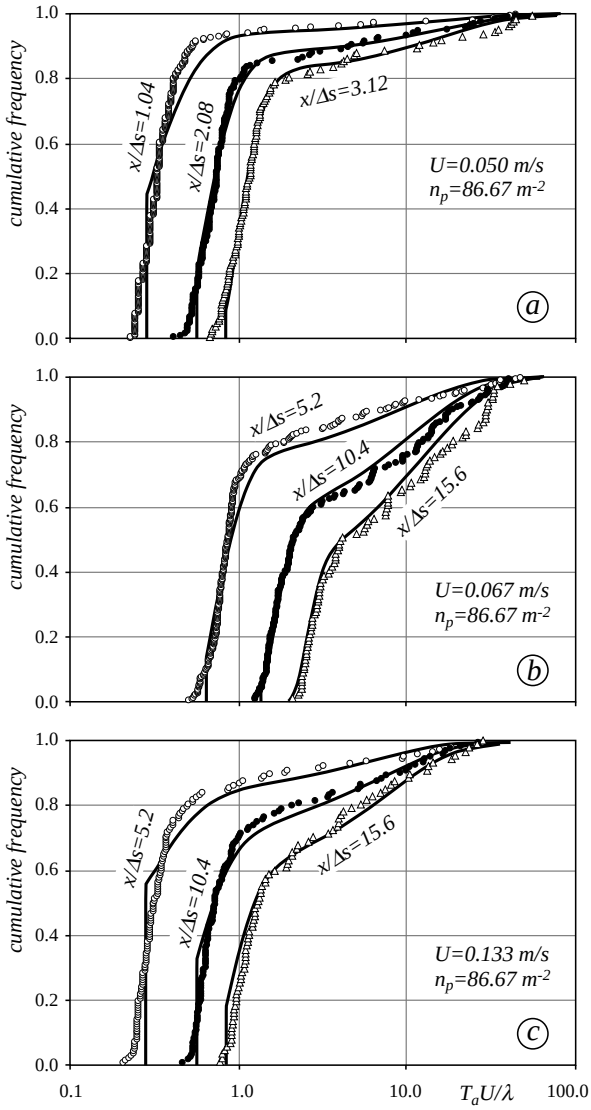

Figure 2.11: Cumulative arrival time distributions: comparison between experimental results (symbols) and model predictions (full line).

The velocity U_0 is the only parameter we adjust in order to fit the experimental data. We observe that in the present experiments (as well as in the experiments in the Section 1.1) the assessed velocity U_0 is, on average, just slightly greater than the bulk flow velocity, and that the difference

$U_0 - U$ decreases with increasing of U (see Table 2.3). We speculate that the relatively large surface velocity U_0 at slow bulk flow velocity is mainly determined by the experimental arrangement.

In fact, at the downstream end of the flume is a weir that concentrates the flow at the free surface; this high velocity layer slowly grows upstream and expands over the whole flow depth.

However the distance upstream from the weir required for a significant vertical mixing is relatively large and increases with decreasing bulk flow velocity.

Indeed, the presence of this high velocity surface layer is possibly the reason why, at low bulk flow velocity, particle velocity u_x in Fig. 2.10 extends well beyond U.

Fig. 2.12 compares the model predictions to the experimental results for experiments A3 and B1 characterized by the same bulk flow velocity of 0.033 m/s and different vegetation density. The cumulative arrival time distributions are computed and measured at the same non dimensional positions $x/\Delta s$ so that, according to the model, the shape of the curves should be exactly the same. However, since the absolute position x of the monitored cross sections are different (see Fig. 2.12), data of experiments B1 are accordingly delayed in time. Experimental data of the two series actually do not overlap perfectly: the sharply rising limb of the curves for experiments A3 have a smaller inclination. This is possibly due to turbulent diffusion which acts over the greater absolute distances travelled by particles in this case.

The comparison shown in Figs. 2.11 and 2.12 indeed serves to provide an indication of whether or not the model includes all the relevant mechanisms responsible for the observed particle dispersion. Therefore, in judging the results one should keep in mind that the computed straight rising limb of the cumulative arrival time distributions, particularly evident in Fig. 2.11a

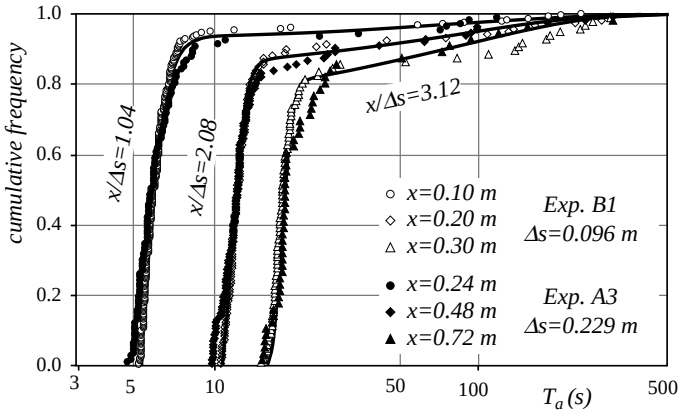

Figure 2.12: Cumulative arrival time distributions: comparison between model predictions (full line) and experimental results for experiments B1 (open symbols) and A3 (full symbols).

and Fig. 2.11c, is determined by particles that reach the monitored cross sections without interacting at all with the vegetation. The comparison could be largely improved by introducing in the model a weak turbulent diffusion, with a diffusion coefficient of the order of 10^{-4} m^2/s. Moreover, the model retention time should include the delay due particle acceleration after the sharp slowdown determined by an interaction event (see fig. 1.8) whereas T_S and T_L given in Table 2.1 are the mean time intervals a particle actually spends at rest. Finally, the average number of interaction events experienced by particles in each run is small and the experimental paths cannot be safely regarded as realizations of a purely random process. At low flow velocity (U=0.033 m/s and U=0.050 m/s) and n_p=86.67 plants/m^2, the mean path length λ=0.22 $\sim$0.28 m is comparably small to the mean centre-to-centre spacing between plants of 0.11 m. Therefore, the experimental arrival time data are not statistically suitable enough to unambiguously serve as a basis for a definitive comparison with the model predictions. Indeed, the discrepancies shown in Fig. 2.11 can be partly ascribed to the irregular morphology of the plants (see Fig. 2.3).

In view of these considerations, we can say that model predictions compare favorably with experimental observations, and that the model actually includes, and correctly describes, all the relevant aspects of the investigated diffusion process.

Chapter 3

Floating particles through emergent cylinders

In the previous experiments described in Section 1.1 we observed the dispersion of floating particles (buoyant seeds) in vegetated open channel flow. The fate of these seeds within a region of vegetation is mainly controlled by the flow velocity, as shown in Section 2.3, and by the efficiency of a variety of seed-plant interaction mechanisms that trap the seeds; the main mechanisms responsible for temporary or permanent trapping of particles observed are: *i*) inertial impaction, which occurs when a particle deviates from a streamline because of its inertia and collides with a stem; *ii*) wake trapping, which occurs when a particle enters the unsteady recirculation zone behind a plant, *iii*) trapping due to surface tension, i.e. the Cheerios effect, in which floating particles are attracted towards stems by the rising meniscus and *iv*) net trapping, which occurs where leaves and/or stems overlap enough to form a netlike structure that intercepts the floating particle.

In particular the last two mechanisms have a strong influence on trapping and on diffusion of floating particles. When the mean gap between leaves or stems is comparable to the particle size, then net trapping is the most efficient trapping mechanism (see Section 2.3). Alternatively, when the mean

gap between plant elements is large compared to the particle size, and flow velocity is moderately slow, then the Cheerios effect is the main, if not the only, mechanism impacting seed propagation, capture and diffusion. The present chapter considers the latter flow condition and develops a physically-based model to predict the impact of surface tension (the Cheerios effect) on the fate of floating particles within a region of emergent vegetation.

Because of it is difficult to distinguish the trapping due to capillarity from trapping due to the net trapping when we use plastic plants, we investigate the issue adopting rigid dowels to mimic vegetation. Since the capillary force is easily evaluable given the geometry and the characteristics of both the particles and the cylinders, a dynamics approach of the problem is encouraged. In particular the effects of the flow velocity on the probability of capture, P_c, and the efficiency of capture of the cylindrical collector are estimated by solving equations that govern the dynamics of floating particle motion. In this work two approaches are developed: *i*) a numerical study focused on the comparison between the efficiency of capture considering only inertial impaction and inertial impaction and the Cheerios effect, and *ii*) a theoretical scheme validated by experimental data collected at the Parsons Lab of the Massachusetts Institute of Technology.

3.1 Efficiency of capture of isolated cylinder at low Reynolds number

Some studies describe the capture mechanisms of particles in suspension by a cylindrical collector that mimics vegetation [*Rubestein and Kohel*, 1977; *Shimeta and Jumars*, 1991; and *Palmer et al.*, 2004]. Originally aerosol filtration mechanisms for particles in suspension have been applied to freshwater [*Silvester and Sleigh*, 1984; *La Barbera*, 1984, and *Brandon and Aggarwal*; 2001]. Specifically the scheme of direct interception to define the

rate of encounter between suspended particles and a cylindrical collector was adopted for sediment and organic matter, e.g. plankton [*Gibbs*, 1985; and *Jackson*, 1989], larvae [*Butman*, 1986] and marine snow [*Alldredge and Gotschalk*, 1988]. The efficiency of capture by direct interception, which is recognized to be the most common encounter mechanism, underestimates the real efficiency observed in these cases for $Re \leq 10$; because others key mechanisms, i.e. inertial impaction and gravitational deposition, have the capture efficiency of the same direct interception order of magnitude, while capture due to diffusion deposition are greater of two orders of magnitude [*Shimeta and Jumars*, 1991].

On the contrary extensive studies focusing on the capture of floating particles are lacking. The capture of floating particles is further affected by the capillary force rising by the free surface deformation [*Kralchevsky and Denkov*, 2001]. The motion of small floating objects due to these forces is affectionately dubbed the "Cheerios effect" and in nature this phenomenon allow the motion of larvae and arthropods on the water surface [*Bush et al.*, 2007], moreover capillarity could be relevant also in the industry to lead the formation of the aggregate in order to simplify the manufacture of components of micro-electromechanical system [*Vella and Mahadeven*, 2005].

In wetlands and riparian communities the Cheerios effect plays an fundamental role in the hydrochory since it affects seed, propagulae, as well as lipid eggs and larvae diffusion and their trapping by plants as shown in the sections 1.1 and 2.3 through their emergent structures, like water reeds (~ 10 mm), plant stems (~ 1 mm) or small hairs ($\sim 0.1 - 0.01$ mm).

The aim of the present Section is investigate how the efficiency of capture changes with stem diameter and particle size at low to moderate Reynolds number ($Re \leq 10$).

3.1.1 Dynamics of interaction particle-cylinder

To determine the capture efficiency we compute the trajectories of small floating particles ($d_p \leq 1$ mm) transported by the flow in the presence of one emergent cylinder (see Fig. 3.1). The particle dynamics is governed by the B.B.O. (Basset-Boussinesq-Oseen) equation [*Umeda and Yang*, 1991] modified to include the attractive force due to capillarity:

$$\left(\frac{\rho_r+\beta}{\rho}\right)\frac{d\tilde{\mathbf{u}}_\mathbf{p}}{d\tilde{t}} = \frac{3\pi C_d}{4\rho_r\tilde{L}_p}\tilde{\mathbf{U}}\left|\tilde{\mathbf{U}}\right| + \left(\frac{1+\beta}{\rho}\right)\frac{d\tilde{\mathbf{u}}_\mathbf{f}}{d\tilde{t}} + \frac{6\tilde{A}_p(\pi\tilde{\nu})^{1/2}}{4\rho_r\tilde{L}_p}\cdot \cdot\int_0^{\tilde{t}}\frac{d\tilde{\mathbf{U}}/d\tilde{t}'}{(\tilde{t}-\tilde{t}')^{1/2}}d\tilde{t}' - \frac{3F_c(\tilde{\mathbf{r}})}{4\pi\tilde{\rho}_p\tilde{d}_p^3} \tag{3.1}$$

here ρ_r is the relative density of the particle given as the ratio of the particle density $\tilde{\rho}_p$ to the water density $\tilde{\rho}$, β is geometric coefficient varying with ρ_r and with the shape of particle (for sphere $\beta = \frac{\tilde{D}_r\tilde{A}_p}{3\tilde{V}_p}$ where $\tilde{D}_r$ is the particle draft, $\tilde{A}_p$ is the waterline area and $\tilde{V}_p$ the total volume of the particle). $\tilde{\mathbf{U}} = \tilde{\mathbf{u}}_f - \tilde{\mathbf{u}}_p$ is the difference between fluid ($\tilde{\mathbf{u}}_f$) and particle velocity ($\tilde{\mathbf{u}}_p$), C_D is the drag coefficient, $\tilde{L}_p$ is the waterline perimeter, $\tilde{\nu}$ is the kinematic viscosity of water, d_p is the particle diameter, $F_c(\tilde{\mathbf{r}})$ is the capillarity force in the radial direction $\mathbf{n_r}$:

$$F_c(\tilde{\mathbf{r}}) = -\frac{\pi\tilde{d}_p\tilde{d}_c\tilde{\sigma}}{2\tilde{l}_c}\sin(\alpha+\psi_p)\sin(\psi_p)\sin(\psi_c)K_1\left(\tilde{r}/\tilde{l}_c\right)\cdot\mathbf{n_r} \tag{3.2}$$

here $\tilde{d}_c$ is the cylinder diameter, $\tilde{l}_c$ is the capillary length, $\tilde{\sigma}$ is the surface tension, and $K_1(x)$ is the first order modified Bessel function. The distance $\tilde{r}$, the contact angle α and the meniscus slopes ψ_p and ψ_c are defined in Fig. 3.1a [*Dushkin et al.*, 1996]. The superscript tildes indicate dimensional variables.

The meniscus angle at contact line of the cylinder ψ_c is related to the contact angle as $\psi_c + \alpha_c = \pi/2$. The meniscus angle at contact line of the

particle ψ_p is estimated by the dynamic analysis of vertical force acting on a floating hydrophilic sphere, as (see Appendix D) [*Joseph et al.*, 2001; and *Kralchevsky and Nagayama*, 2000]

$$\sin(\alpha+\psi_p)\sin(\psi_p) + Bo\left[\frac{\rho_r}{6} - \frac{2+3\cos(\alpha+\psi_p)-\cos^3(\alpha+\psi_p)}{24} + \right.$$
$$\left. + \frac{\sin^3(\alpha+\psi_p)\sin(\psi_p)K_0\left(\frac{\tilde{d}_p}{2\tilde{l}_c}\sin(\alpha+\psi_p)\right)}{8}\right] = 0 \quad (3.3)$$

where $Bo = \tilde{\rho} g \tilde{d}_p^2/\tilde{\sigma}$ is the Bond number of the particle, and $K_0(x)$ is the modified Bessel function of order zero. The leftmost term is the vertical contribution of the surface tension; the terms inside the square brackets describe, from left to right, the gravitational force on the sphere, the pressure contribution (i.e. Archimedean force) and the reduction of buoyancy due to the depression generated by the rising of meniscus around the sphere.

In Eq. 3.1 the first term on the right hand side is the drag term ($\mathbf{F_d}$), the second one is the added mass, and third term (the memory term) represents the force associated with past movements of the particle. Eq. 3.1 can be rearranged to read:

$$\frac{d\mathbf{u_p}}{dt} = \frac{3\,|\mathbf{U}|}{4(\rho_r+\beta)R}\left[\frac{24}{Re\,|\mathbf{U}|\,R} + \frac{6}{\sqrt{Re\,|\mathbf{U}|\,R}} + 0.4\right]\mathbf{U} +$$
$$-\frac{3}{We\cdot\ R^2}\sin(\alpha+\psi_p)\sin(\psi_p)\sin(\psi_c)K_1(r)\cdot\mathbf{n_r} \quad (3.4)$$

where $R = d_p/d_c$ with $d_p = \tilde{d}_p/\tilde{l}_c$ and $d_c = \tilde{d}_c/\tilde{l}_c$, $Re = \tilde{d}_c\cdot\tilde{u}_0/\tilde{\nu}$ is the Reynolds number and $We = \tilde{\rho}\cdot\tilde{d}_c\cdot\tilde{u}_0^2/\tilde{\sigma}$ is the Weber number. All velocities are nondimensionalized by $\tilde{u}_0$ and the time by $\tilde{d}_c/\tilde{u}_0$. In eq. 3.4 the added mass term and the memory term are neglected since the Stokes number $S = R^2\cdot\rho_r\cdot Re/18$ is small enough [*Barton*, 1995] and the term between square brackets is an approximation of the drag coefficient for $Re < 2\cdot 10^5$ (*White*, 1991).

To solve Equation 3.4 we need to reconstruct the flow field generated by the presence of one emergent cylinder in an otherwise uniform open channel flow. To solve this problem we use the computational fluid dynamics code using finite elements method, COMSOL multiphysics.

Once the velocity pattern is computed, Eq. 3.4 is solved numerically by a backward Euler scheme (see Appendix E).

3.1.2 Numerical investigations

Particle trajectories are controlled by a large number of variables (Re, We, Bo, R, ρ_r, α and ψ_c). In the simulations we assumed the fluid to be water (i.e $\tilde{\rho}$ =1000 kg/m^3, $\tilde{\nu}$ =10^{-6} m^2/s, $\tilde{l}_c \approx 2.7$ mm for water and $\tilde{\sigma} \approx 0.073$ N/m) and computed the efficiency of capture as it is affected by flow velocity, cylinder diameter, and particle size and density.

An example of particle trajectory for d_c=1.0, d_p=0.1, ρ_r=0.7 and Re=1 is given in Figure 3.1b. Trajectories of particles starting upstream from the cylinder, along the segment b, cover the area hatched with gray in Fig. 3.1b. Particles that follow these trajectories all go stuck against the cylinder and are captured. Differently from the case of direct interception of suspended particles, the backside portion of the collector also contains stuck particles and contributes to enhance the efficiency of capture defined as $\eta = b/d_c$ [*Palmer et al.*, 2004]. Particles that start outside the segment b, follow trajectories that lie outside the hatched area and are not captured.

Fig 3.2 shows how the efficiency of capture due to direct interception η_D and the total efficiency η which includes the Cheerios effect, vary with Reynolds number, when the particle and cylinder diameters are leaved unchanged (R=0.1). We observe that η_D increases with Re, i.e., with flow velocity: this behavior is promoted by the streamlines that pass closer to the cylinder, thus promoting the particle trajectories which impact to the cylinder. Moreover, since the cylinder diameter is relatively large, η_D turns

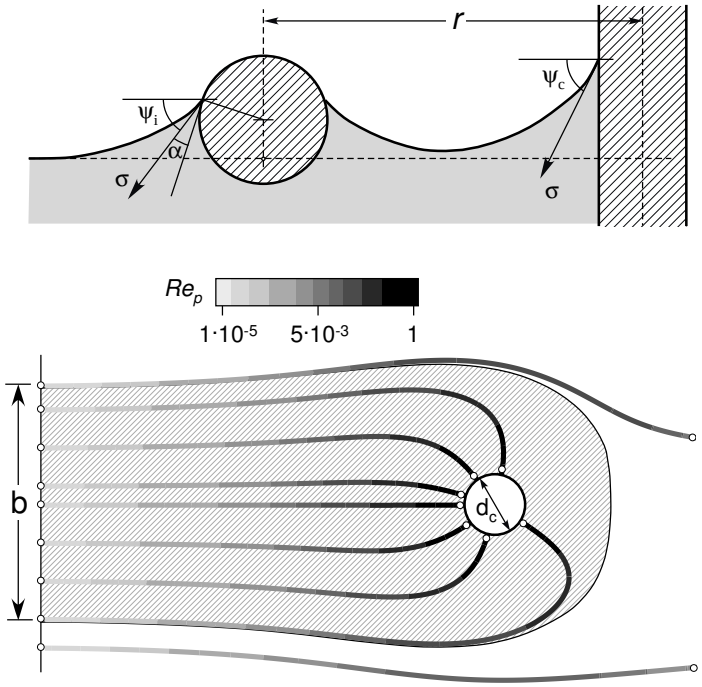

Figure 3.1: *a*) The definition of menisci and contact angle. *b*) Floating particle trajectories in the presence of a cylinder (Re=1, d_c=1.0, d_p=0.1, ρ_r=0.7, ψ_c = 80°, and α = 60°). In all cases the particles is accelerated by capillarity as they approach the cylinder (Re_p is the Reynolds number of the relative motion of the particle with respect to the flow).

out to be negligibly small compared to the total efficiency. In this case, efficiency is primarily controlled by the ratio of inertia to capillarity which increases with flow velocity ($We \propto Re^2$), and only particles which flow close to the cylinder can be captured.

We then study how the efficiency vary with cylinder diameter and particle size and density for a given Reynolds number; in this case $We \propto 1/d_c$. Fig. 3.3.a shows the capture efficiency as a function of cylinder diameter for a given particle size.

To explain the behavior we consider a particle trajectory which starts at a given distance δ (δ/d_c=const.) in the transverse direction (see fig. 3.3.c).

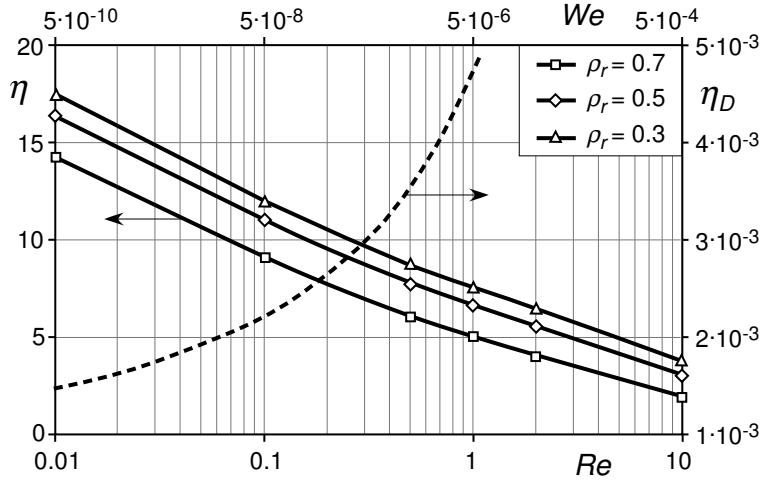

Figure 3.2: The efficiency of capture η as function of Re for three different particles densities (full lines with symbols). The dashed line is the efficiency of capture η_D due to direct interception [*Palmer et al.*, 2004]. In the computations we used $d_c = 1.0$, $d_p = 0.1$, $\psi_c = 80°$, and $\alpha = 60°$.

For very small d_c (d_c <0.2 in fig 3.3a) the particle is strongly attracted toward the cylinder by the capillary force, in fact its distance r is small (fig. 3.3c$_1$). However, We is very large and inertia turns out to be much greater than capillary force. For this reason the efficiency of capillary force is negligibly small.

For moderately small cylinder diameter (Fig. 3.3c$_2$), capillary force is much stronger and, although the distance r of the particle from the cylinder is relatively large, the attractive force due to capillarity is large compared to inertia and the capture efficiency is enhanced.

For relatively large cylinder diameter (fig. 3.3c$_3$), capillarity force is further increased, inertia is relatively small, however the particle distance r is very large so that the attraction force, controlled by $K_1(r)$, is relatively weak at this large distance.

On the whole, the efficiency determined by solely the capillarity attraction is negligibly small at very small and large cylinder diameter and exhibit

a maximum at intermediate cylinder size. However, the total efficiency includes inertia impaction and direct interception which are large at very small d_c and decreases with increasing d_c (fig. 3.3a). The combination of all these capture mechanisms then determines the behavior shown in Fig. 3.3.

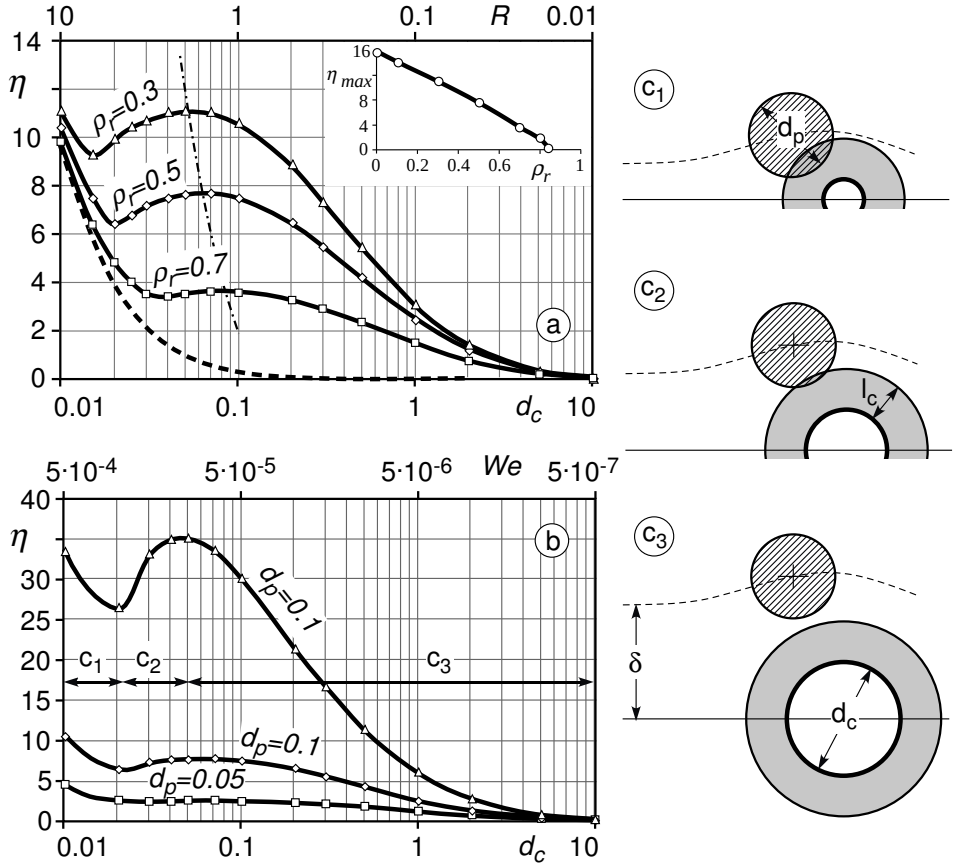

Figure 3.3: Efficiency of capture η as function of d_c for $Re = 1$ and ψ_c=5°: *a*) efficiency for three different values of particle density and d_p=0.1, α=60°; the dashed line gives the efficiency of solely direct interception; *b*) efficiency for three different values of particle diameter and ρ_r=0.5, α=60°; *c*) particle-cylinder interaction characteristics for very small (upper panel), moderately small (middle panel) and large (lower panel) cylinder diameter.

It is worth noting that the most common mechanisms of encounter for suspended particles, i.e., direct interception and inertial impaction, signifi-

cantly underestimate the actual efficiency when particles are floating.

Particle density (ρ_r) and size (d_p) mainly controls the intensity of efficiency through affecting the inertia. By reducing the density of lighter than water particles (ρ_r <1) inertia decreases and the capillarity force increases. The latter is because, by reducing of ρ_r, the meniscus angle at contact line ψ_p increases significantly (see eq. 3.3). Therefore, on the whole, the efficiency η decreases with ρ_r (Fig. 3.3a).

On the contrary, by increasing particle size, inertia increases but also capillary force increases, due the increase of the meniscus angle at the contact line ψ_p. Since the increase of capillary force is stronger than that of inertia, on the whole, and to some extent counter-intuitively, the efficiency of capture η increases with particle size (fig. 3.3b).

We can summarize the above discussion stating that capture efficiency is basically governed by the relation between inertia and capillary force. The same apply when studying the distribution of captured particles along the cylinder surface.

At very small d_c, we see (Fig. 3.3) that capillary force is not effective, but the efficiency is large because of the large contribution due to direct impaction. We then expect that captured particles gather in the frontal part of the cylinder. This is confirmed by the results of the numerical simulations (Fig. 3.4.1).

For moderately small cylinder diameter, capture efficiency, which is mainly due to capillarity attraction, attain a maximum (Fig. 3.4). In this case, particle starting near the ends of segment b in Fig. 3.1, due to the strong attraction promoted by capillarity, after bypassing the cylinder flow backward and gets stuck against the back face of the collector (Fig. 3.4.2-3).

Further increasing of cylinder diameter, as previously discussed, reduces the capture efficiency due to capillarity and the probability a particle gets stuck in the rear of the cylinder decreases (Fig. 3.4.4-5). On the whole, the

larger the efficiency the more uniform the distribution of particles along the cylinder surface.

Therefore, uniformity in the distribution of stuck particles along the cylinder surface is actually a measure of the capture efficiency. Interestingly, the more uniform the distribution of particles along the cylinder surface the more room is available to particles for getting stuck, and more particles are actually captured by the collector.

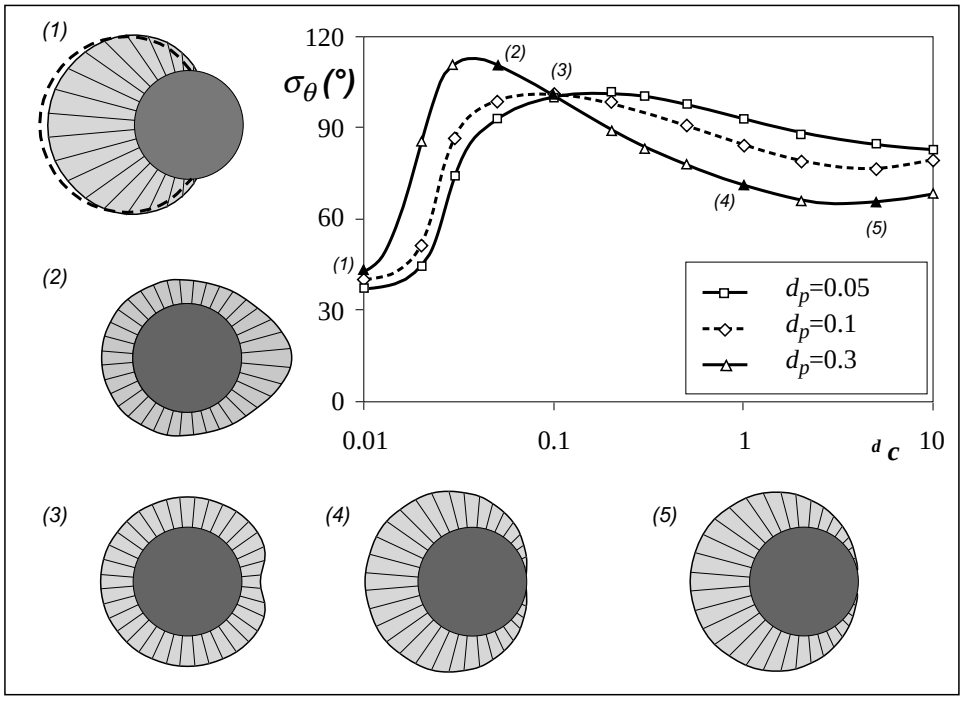

Figure 3.4: Variance of the angular distribution of captured particles as a function of cylinder diameter for the three different particle sizes shown in fig. 3.3b (Re=1, ψ_c=5°, ρ_r=0.5 and α=60°). In the scheme 1-5 frequency of capture around the collector of the particle with d_p=0.3 for five different cylinder size d_c.

3.2 The capillary trapping of buoyant particles flowing through an array of cylinders

The model shown in the previous section is an effective tool to evaluate the capture of floating particle by a cylindrical collector. However the numerical solution adopted is not straightforward in the presence of an array of cylinders and for large Reynolds number (Re>10). In this case *i*) we need to average the efficiency in time because of the unsteady flow condition due to the vortex shedding at downstream of the cylinder; *ii*) cylinders induced a strong turbulence within the canopy and the computational cost to solve the hydrodynamics of the problem increases; and *iii*) the model cannot describe the fate of a particle after it collides with the cylinder. Therefore, although the use of the proposed numerical model can be extended above Re=10, the devices required for the solution need to be improve.

In this section, we propose a theoretical scheme based on a kinematic approach and validate the scheme through experimental investigations at moderate Reynolds number. The aim of this study is model the particle-cylinder interaction processes and permanent capture observed when the effects of capillarity prevails on other interaction mechanisms.

3.2.1 kinematic model to predict particle trapping

The emergent vegetation is simulated as an array of randomly-arranged cylinders, with diameter d_c. The array density is given by the cylinders per unit area, n_c. The cylinder spacing is assumed to be far greater than the particle size, which eliminates net trapping, i.e. the trapping of particles between a pair of cylinders. In this case the capture of floating particles by the cylinders is dominated by inertial impaction [*Palmer et al.*, 2004] and by the attraction due to the surface tension (i.e., the Cheerios effect).

As a particle advects through the array of cylinders, it passes, on average,

one cylinder within each longitudinal distance, $\Delta s = (n_c d_c)^{-1}$, as shown in Section 2.2. As each cylinder is passed, the particle has some probably of colliding with it, P_i, so that on average a particle will interact (collide) with a cylinder once per distance is

$$\Delta S_i = \frac{\Delta s}{P_i} = \frac{1}{n_c \cdot d_c \cdot P_i} \tag{3.5}$$

Except for the extreme cases (i.e. for high cylinder density or very low flow velocity) we expect that the probability P_i does not depend on n. Preliminary experiments, discussed in Section 3.2.2, confirm this.

Observations have shown that particles may collide (interact) with several cylinders, before being captured by, i.e. permanently attaching to, a specific cylinder (as in the experiments in Chapters 1 and 2). Based on this, we separately define the process of interaction (collision followed by release) and the process of capture (permanent trapping).

Following Eq. 1.2, we define the probability $P(X > L)$ that a particle travels a distance X greater than L before being captured, as:

$$P(X > L) = (1 - P_c)^{N_i} \tag{3.6}$$

where P_c is the capture probability (i.e., the probability that a particle, which interacts with a cylinder, is permanently captured), and N_i in the number of interactions between a particle and the cylinders within the distance L, which we approximate as $N_i = L/\Delta s_i$. We can rewrite Eq. 3.6 as

$$P(X > L) = e^{-L/\lambda} \tag{3.7}$$

in which

$$\lambda = -\frac{\Delta S_i}{\ln(1 - P_c)} \tag{3.8}$$

is the mean distance travelled by a particle before it is permanently captured.

In order to estimate P_i, and thus Δs_i, we consider the trajectory of individual particles as they pass an individual cylinder (Fig. 3.5). For example, to describe inertial impaction, previous authors assumed that the particle trajectory was set by the fluid drag and particle inertia. A set of trajectories associated with these assumptions is shown in Fig. 3.5a. The length-scale b is the distance between the outermost trajectories, relative to the centerline, that lead to collision. Geometrically, $P_i = b/d$ (Fig. 3.5). Models to predict b, and thus P_i, for inertial impaction are described in *Shimeta and Jumars* (1991) and *Palmer et al.* (2004).

However, in this section we focus on floating particles at low flow velocity, for which the acceleration promoted by surface tension (i.e. Cheerios effect) can be important, drawing particles towards the cylinder from distances greater than d. An example of trajectories for surface particles influenced by surface tension is shown in Fig. 3.5b. Because it is possible for $b > d$ as shown in Section 3.1.2, the probability of collision P_i can be greater than one. While this sounds contradictory, it is physically sound. It characterizes the fact that the influence of surface tension can generate more frequent cylinder collisions than would be predicted from the mean spacing, i.e. $\Delta s_i < \Delta s$. In the next section we develop a model to predict b, and thus P_i, for floating particles influenced by surface tension (Fig. 3.5, lower panel).

Theoretical prediction of P_i for floating particles under the influence of surface tension

The Cheerios effect is influenced by the relative importance of inertial forces and surface tension. However, these two forces act on the particle in different directions, so that P_i cannot be parameterized simply by the ratio of the force magnitudes. Instead, we use a kinematic approach for defining P_i. For this description x and z are the streamwise and transverse coordinate

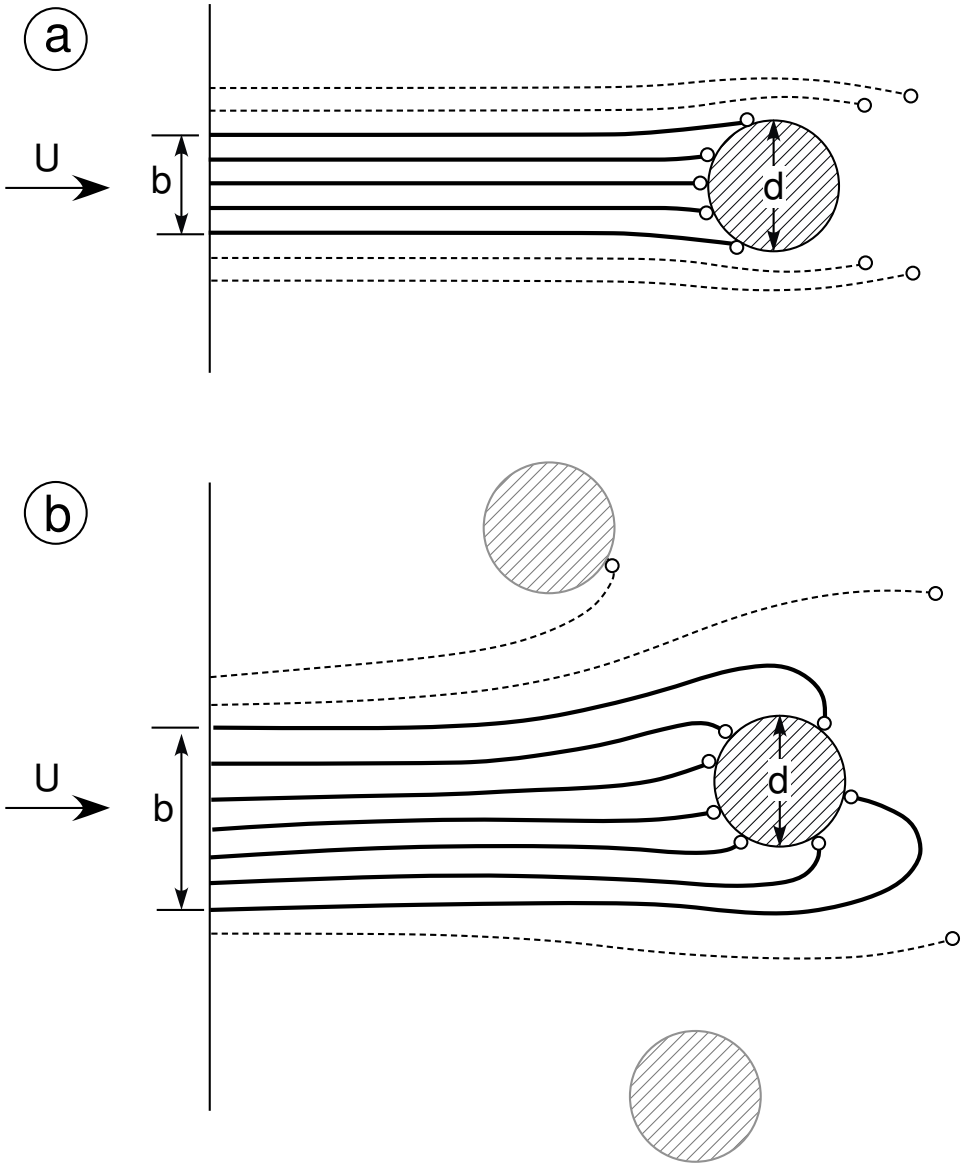

Figure 3.5: Definition sketch for the probability of particle collision (interaction) with a cylinder of diameter d. Solid lines indicate particle trajectories that lead to collision. The outermost trajectories that lead to collision are separated by distance b. The collision probability is $P_i = b/d$. *a*) inertial impaction occurs when the forces of drag and inertia dominate the particle trajectory approaching the cylinder. *b*) For floating particles, the Cheerios effect adds to inertia and drag in controlling the particle trajectory. The definition of b for this case is developed below.

directions, respectively (Fig. 3.6). We define a square area of influence, centered at the cylinder, whose edge is the capillary length, now defined as $1/q$, and we assume that a particle crossing this area is attracted toward the cylinder through the Cheerios effect. If we assume that the particles move, on average, at the bulk velocity U, then, on average, a particle will spend time $T_q = \beta_q/(qU)$, within the zone of influence. We introduce the scale constant β_q to account for the assumption of a square zone of influence, when in fact the meniscus is distributed radially around the cylinder. T_q is also the time available for the Cheerios effect to draw a particle to the cylinder, before it leaves the influence of the cylinder. From this time-scale we can estimate the maximum distance from the cylinder, H_0, from which a particle can be drawn to collide with the cylinder by the action of surface tension (see Fig. 3.6).

This maximum distance corresponds to $b/2$ of Fig. 3.5, i.e., $b = 2H_0$ and

$$P_i = 2H_0/d \tag{3.9}$$

The distance H_0 is computed, as a first approximation, by assuming that only the capillary force acts on both the particle and the cylinder. The particle is assumed to be spherical. The capillary force, F_c, given by Eq. 3.2 is rewritten as

$$F_c = -\frac{\pi}{2} \cdot d_p \cdot d_c \cdot q \cdot \sigma \cdot \sin(\alpha + \psi_p) \sin(\psi_p) \sin(\psi_c) K_1(qz) \tag{3.10}$$

with respect to eq. 3.2 dimensional variables are written without tilde and z is the transverse distance of the particle from the cylinder.

The following differential equation governs the particle position, z,

$$\frac{d^2(qz)}{dt^2} = cK_1(qz) \tag{3.11}$$

with

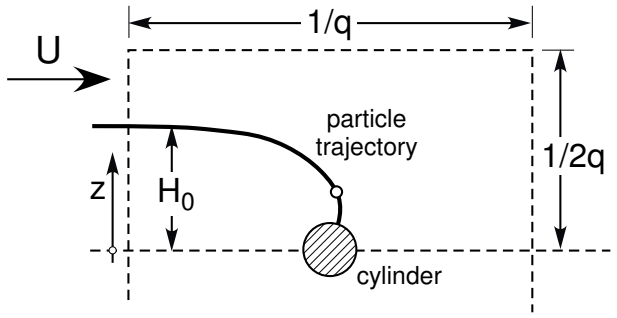

Figure 3.6: A particle trajectory influenced by surface tension and which leads to collision with the cylinder. H_0 represents the maximum distance from the cylinder from which a particle can be drawn to collide with the cylinder by the action of surface tension.

$$c = \frac{3d_c\sigma q^2}{\rho_p {d_p}^2}\sin(\alpha+\psi_p)\sin(\psi_p)\sin(\psi_c) \tag{3.12}$$

We assume that the particle starts from rest at position $z = Ho$, i.e. boundary conditions

$$t = 0 \begin{cases} z = H_0 \\ \\ dz/dt = 0 \end{cases} \tag{3.13}$$

The solution to Eq. 3.13 is approximated as

$$qz = \sqrt{(qH_0)^2 - c(qH_0)^{-2}t^2} \tag{3.14}$$

The maximum distance, H_0, will be that associated with the maximum time available for lateral transport driven by surface tension, that is T_q. For simplicity, we assume that the particle collides with the cylinder at $z = 0$. Then, setting $z = 0$ and $t = T_q$, we solve eq. 3.14 for H_0

$$H_0^2 = \beta_q \frac{\sqrt{c}}{Uq^3} \tag{3.15}$$

Using Eqs. 3.9, 3.12 and 3.15 we find

$$P_i = \frac{2H_0}{d_c} = \frac{2\sqrt{\beta_q}}{d_c q\sqrt{U}}\left[\frac{3d_c\sigma}{\rho_p d_p^2}\right]^{1/4}[\sin(\alpha+\psi_p)\sin(\psi_p)\sin(\psi_c)]^{1/4} \tag{3.16}$$

Since $We = \rho \cdot d_c \cdot U^2/\sigma$ is the Weber number, Eq. 3.16 can be rewritten as

$$P_i = \frac{\beta}{d_c q We^{1/4}}\sqrt{\frac{d_c}{d_p}}\left(\frac{\rho}{\rho_p}\right)^{1/4}[\sin(\alpha+\psi_p)\sin(\psi_p)\sin(\psi_c)]^{1/4} \tag{3.17}$$

where $\beta = 3^{1/4}2\sqrt{\beta_q}$. Experiments described in Section 3.2.2 suggest β=2.46, such that β_q=0.87, which is close to unity, as expected.

Capture probability P_c

After a particle collides with a cylinder, it may become permanently attached, or it may be pulled away from the cylinder by the action of fluid drag. The probability of remaining permanently attached, P_c, depends on the ratio between the capillary force acting when the particle is stuck to the cylinder and the drag force due to the local mean flow, to turbulence and to vortex shedding. We assume that this drag force F_d, is proportional to the bulk velocity, U.

$$F_d = k_d C_d \rho A_p U^2 \tag{3.18}$$

where k_d is a scale factor, A_p is the particle area invested by the flow and C_d is the particle drag coefficient.

When the ratio of capillary force (Eq. 3.10) to drag force (Eq. 3.18) is large, the particle remains attached to the cylinder, i.e. P_c=1.0. We define E_{cr} as the critical value of this force ratio above for which the probability of capture become unity, P_c=1 i.e.,

$$E_{cr} = \left.\frac{F_c}{F_d}\right|_{P_c=1} = -\frac{\pi}{2}\frac{d_p d_c \sigma q}{k_d C_d \rho A_p U_e^2}\sin(\alpha+\psi_p)\sin(\psi_p)\sin(\psi_c)K_1\left(q\frac{d_p+d_c}{2}\right) \tag{3.19}$$

in which we define U_e as the escape velocity, i.e. the velocity above which particles may escape from the cylinder. We introduce the shape factor, k_p, such that $A_p = k_p d_p^2$, then rearrange Eq. 3.19 to describe the escape velocity, to

$$U_e^2 = \beta_e \frac{d_c}{d_p}\frac{\sigma q/\rho}{k_p C_d}\sin(\alpha+\psi_p)\sin(\psi_p)\sin(\psi_c)K_1\left(q\frac{d_p+d_c}{2}\right) \tag{3.20}$$

with

$$\beta_e = \frac{\pi}{2E_{cr}k_d} \tag{3.21}$$

which we will use as a calibration parameter. Experimental investigations described and discussed in Section 3.1.2 suggest β_e=1.26.

The escape velocity U_e is the scale velocity of the problem. When $U \leq U_e$ the capillary force is greater than drag forces no matter the position (with respect to the mean flow) at which the particle is stuck to the cylinder, therefore the probability of permanent capture is $P_c = 1$. When $U > U_e$, drag forces may locally and temporarily exceed the attraction force due to capillarity, and the particle may escape from the cylinder. Increasing of the ratio U/U_e reduces the probability P_c.

The measurements, discussed below, suggest that the probability of capture P_c decays exponentially with U/U_e, specifically

$$P_c = \begin{cases} 1 & U/U_e \leq 1 \\ \\ e^{1-U/U_e} & U/U_e > 1 \end{cases} \tag{3.22}$$

From the models developed above we can now predict the following from the particle characteristics (d_p), the cylinder diameter (d_c), the stem density

(n_c), and the bulk flow velocity, U: i) the the mean spacing between two interactions Δs_i from Eqs. 3.5 and 3.17, ii) the escape velocity U_e from Eq 3.20, the capture probability P_c from Eq. 3.22, iii) the mean distance a particle travels before it is permanently captured, λ, from Eq. 3.7, and iv) the path length distribution $P(X > L)$ from Eq. 3.6. In the next section we use experimental observations to evaluate the two model parameters, β=2.46 and β_e=1.26.

3.2.2 Experimental results

To cover a wider range of flow conditions, two flumes are used in this investigation. The small flume has a channel width of 40 cm and length of 2.8 m, the large flume has a width of 120 cm and length of 13 m. In both flumes the water is recirculated by a pump that maintains steady flow. Both flumes have a fixed horizontal bottom, and the water depth can be adjusted by a downstream weir. In the small flume the bulk flow velocity U is measured with an ADV (U is averaged over 33 points per cross section), while in the large flume U was estimated through a calibrated relationship between the pump frequency and the flow rate. The bulk velocity was varied between 0.7 and 5.0 cm/s. Seven of the velocity experiments were carried out in the small flume (0.007-0.032 m/s), while higher velocity experiments (U = 0.04 and U = 0.05 m/s) were carried out in the large flume. In both flumes, a random array of cylinders was constructed on three boards to create a total test section length of 1.80 m. The array filled the flume width. We constructed six different arrays, with n_c = 299 m^{-2} to 1780 m^{-2}. . The cylinders used in the experiments are wooden dowels with a diameter d_c of 6.0 mm, fitted into holes drilled into the boards.

The model floating particles were cut from wood cylinders to have equal diameter and height of 3 mm. The relative density was ≈0.7. These are the same as particle C used in the experiments shown in Chapter 2.

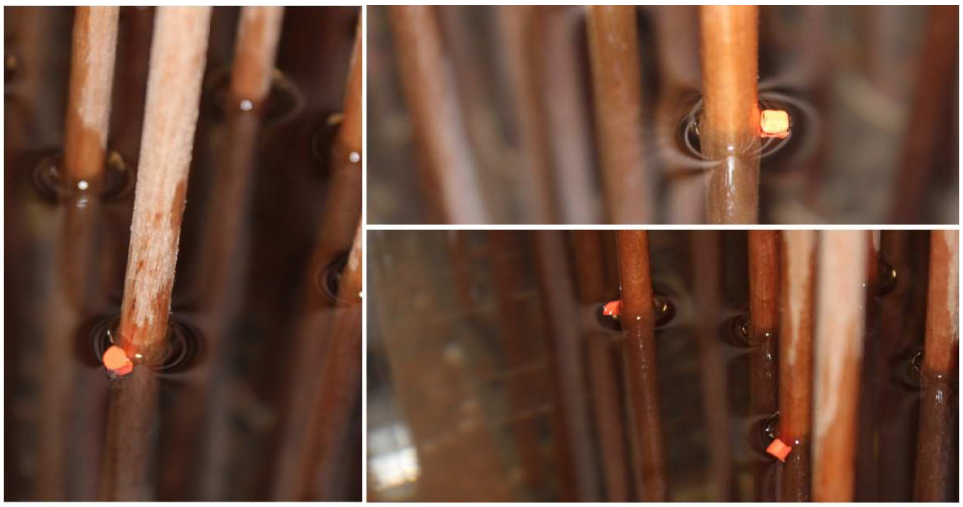

Figure 3.7: Trapping of floating wood cylinders (particle C) by emergent dowels array by the Cheerios effect.

In the experiments, we release one particle at a time just upstream of the test section and at random positions in the transverse direction. For each experiment we released 200 particles. We observed the particle trajectory and measured the distance travelled by each particle before it was permanently captured by a cylinder. We assumed a particle was permanently captured if it stayed stuck to one cylinder for more than 10 min, a time interval that was more than one order of magnitude longer than than the mean time a particle took to travel the whole test section (see Fig. 3.7).

We first consider the impact of cylinder density, n_c, while holding the bulk velocity constant (U=2.5 cm/s). In all cases the exponential distribution given by Eq. 3.6 could be fit to experimental data with R^2 >0.95. From this fit we extracted the mean path length, λ, for each stem density. From our theory, we expected that λ would have a dependence on the stem spacing, $\Delta s = (n_c d_c)^{-1}$. This relationship is observed in the measured (Fig. 3.8). The data indicate a constant relationship between λ and n_c^{-1}, specifically $\lambda = 230/n_c$ for the present data (Figure 3.8, black circles). Since n_c is a constant, from Eqs. 3.1 and 3.3 together, we can infer that the product

$P_i ln(1 - P_c)$ is also a constant. Consistent with the derivation above, we expect that the probability P_c is only a function of the flow near an individual cylinder, and that it does not depend on cylinder density, n_c. Then, P_i must also be independent of n_c.

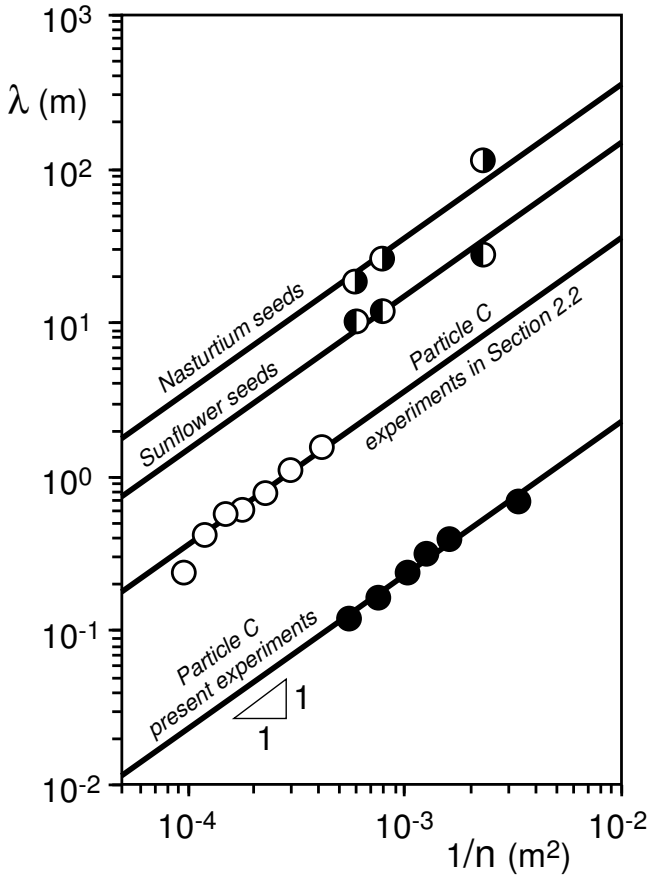

Figure 3.8: Mean path length as a function $1/n_c$. Present experimental results (black circles aligned along the curve $\lambda = 230/n_c$); experimental results in Section 2.2 with particle C and U=0.033 m/s (white circles, $\lambda = 3600/n_c$); and (half-full symbols) experimental data for Nasturtium ($\lambda = 3.5 \cdot 10^4/n_c$) and Sunflower seeds ($\lambda = 1.5 \cdot 10^4/n_c$) [Chambert and James, 2009].

Further experiments were carried out with the aim of investigating how the model parameters change with the bulk flow velocity, U. The distance travelled by 200 particles is measured for n_c=968 m^{-2} and nine different

flow velocities (see Tab. 3.1). In each case, the probability distribution of distances traveled by a particle before permanent capture followed an exponential law with R^2 >0.95, except for the data with U=0.040 m/s where, possibly because of the presence of a weak transverse seiche in the channel, the determination coefficient was lower (R^2=0.90), but still highly significant. Again, the exponential fit was used to determine the mean path length, λ, and to observe how this parameter varied with bulk flow velocity (see Tab. 3.1).

Using the set of nine (U, λ) pairs, we calibrated the model parameters β and β_e. First, we used the following trial and error procedure to find β. We fixed a tentative value for β and used it to compute the probability of interaction, P_i, from Eq. 3.17, which in turn is used to find the mean spacing between interactions Δs_i from Eqs. 3.5 and 3.17. Together with the observed λ, we find the capture probability P_c from Eq. 3.8. With nine pairs of (P_c, U), we find U_e by fitting Eq. 3.22. The value for β is then tuned to until we find the best fit to Eq. 3.22. Second, using the best-fit value for β, β_e is computed from Eq. 3.20. In this computation we used d_p=0.003 m, ρ_r= 0.7 and the contact angles $\alpha = 60°$ and $\alpha_c = 55°$ for the particles and the cylinder, respectively. We computed ψ_p=1.55° (see Appendix D) and ψ_c= 90° - α_c = 35°. Through this procedure we find β=2.46 and β_e=1.26. With these values, the interaction probability P_i, the mean spacing Δs_i, and the probability P_c are computed as given in Tab. 3.1. The comparison between computed (Eq. 3.22) and measured values for the probability P_c is shown in Fig. 3.9, where the escape velocity, from Eq. 3.20, is U_e=0.013 m/s.

We now can use experimental results provided in Sections 1.3 and 2.3, and by *Chambert and James* [2009] to validate the model. These cases consider particle sizes and stem diameters which are different from those in the present study.

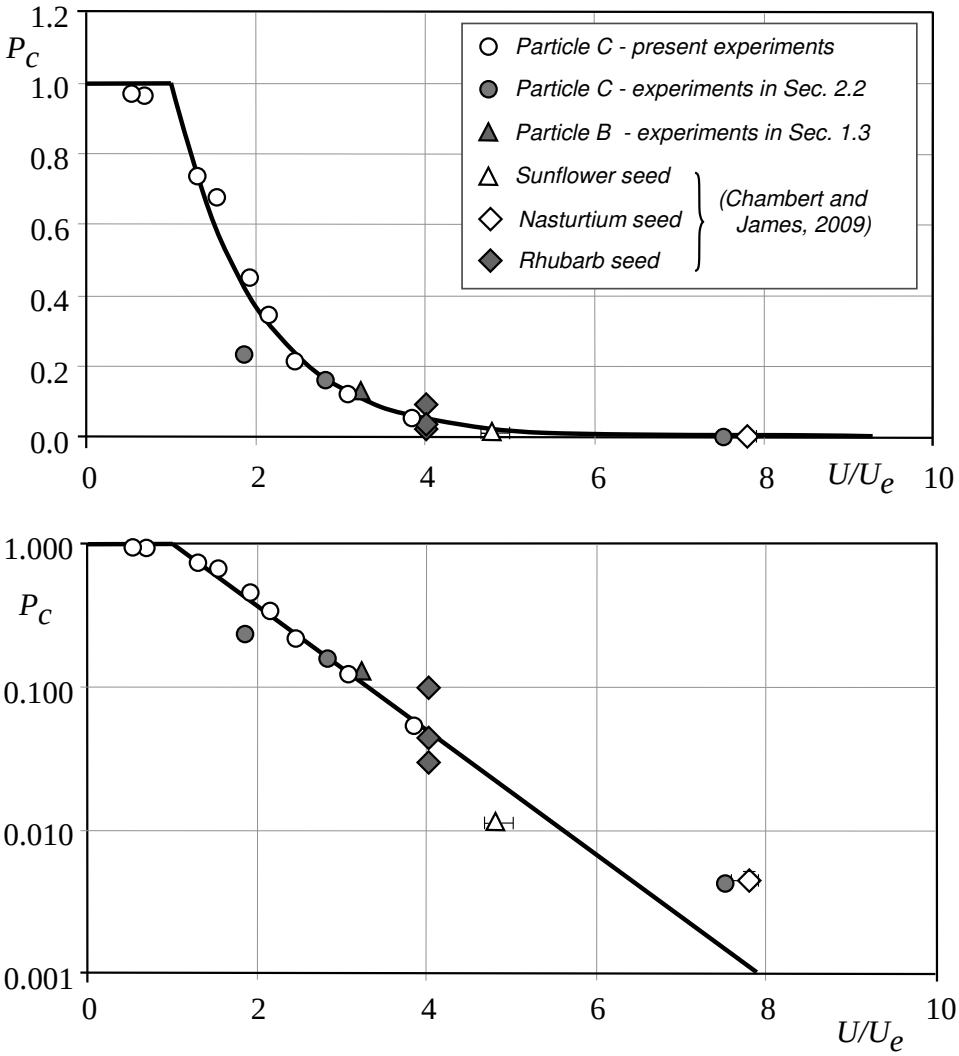

Figure 3.9: Comparison between theoretical and experimental probability of capture as it varies with U/U_e. The capture probability is plotted both in natural scale (upper panel) and logarithmic scale (lower panel).

Table 3.1: Summary of present experimental data and model parameters.

$U\,(m/s)$	$We\,(\cdot 10^2)$	Re	P_i	$\Delta s_i\,(m)$	$\lambda\,(m)$	P_c
0.007	0.403	42	2.32	0.074	0.021	0.971
0.009	0.666	54	2.05	0.084	0.025	0.965
0.017	2.380	102	1.49	0.116	0.086	0.739
0.020	3.290	120	1.37	0.125	0.110	0.680
0.025	5.140	150	1.23	0.140	0.234	0.451
0.028	6.440	168	1.16	0.148	0.353	0.343
0.032	8.420	192	1.09	0.159	0.642	0.219
0.040	13.200	240	0.97	0.177	1.357	0.122
0.050	20.500	300	0.87	0.198	3.549	0.054

Here, we tentatively assume that each leaf piercing the free surface in the plastic plants used in the previous chapters can be represented as a cylinder having a diameter of 2 mm, which corresponds to the larger dimension of the leaf, which has an elliptical cross-section. This leaf diameter is smaller than the particle diameter, d_p (see Fig. 2.1).

For particle C, in Section 2.2 showed that the mean path length λ varied inversely with the number of plants per unit area (Fig. 2.6). Since each plant had the same number of leaves (i.e. 120), the mean path length also varies inversely with the number of leaves (i.e., cylinders) per unit area, as shown in Fig. 3.8.

In the experimental investigation shown in Chapter 1, individual leaves were, in some places, spaced closely enough to create net trapping, so that the probability of capture, P_c, measured in those studies reflects both the net trapping and the trapping associated with the Cheerios effect. The

theory presented here only accounts for the Cheerios effect, and so we must isolate that mechanism from the data reported in Section 1.3. We assume that the probability of capture due solely to the Cheerios effect is given by the measured total probability of capture (which includes the net trapping mechanism) times the measured percentage of captures due to the Cheerios effect, which is reported in Section 2.3. Moreover, for the plastic leaves we measured a contact angle $\alpha_c \approx 30°$ so that $\psi_c = 90°$ - $\alpha_c \approx 60°$. Experimental data as well as the results of the computations are given in Tab. 3.2.

Table 3.2: Summary of experimental conditions shown in Chapters 1 and 2 and the results of present computations.

particle	$d_p\,(mm)$	ρ_p/ρ	$\alpha\,(°)$	$\psi_p\,(°)$	$U\,(m/s)$	$U_e\,(m/s)$	P_c
A	2.5	0.95	–	–	0.073	–	–
A	2.5	0.95	–	–	0.081	–	–
B	3.7	0.83	35	3.55	0.073	0.020	0.13
C	3.0	0.70	60	1.55	0.033	0.016	0.24
C	3.0	0.70	60	1.55	0.050	0.016	0.16
C	3.0	0.70	60	1.55	0.133	0.016	0.02

The measured values of P_c and U/U_e reported in Tab. 3.2 are included in Fig. 3.9. The data points collected in the previous experiments are consistent with the model curve (solid line) developed for an array of cylinders. This agreement is encouraging, especially given the rather different experimental conditions and possible uncertainties, e.g., *Spartina* leaves are not cylinders, some of the net-trapping captures may actually have been through the Cheerios effect, i.e. net trapping may mask some of the captures through the Cheerios effect. These experimental results suggest that the relationships proposed to estimate the model parameters when the Cheerios effect is the

dominant capture mechanism, can be extended, with the due care, to real plants. In this connection, an allometric study to establish the equivalence between a real plant and the diameter and density of a group of cylinders could be of use.

Chambert and James [2009] experiments were conducted in a 20 m long and 0.38 m wide flume. The model vegetation comprised an array of cylinders with a diameter of 0.006 m, arranged across the full width of the flume in staggered pattern. The total array length was 1.88 m, and the array began 1 m downstream from the seed feeder.

Three sets of experiments were carried out with the three different stem densities and same mean flow velocity, U=0.16 m/s. Five types of natural, buoyant seeds were used for the experiments: *African daisy*, *Nasturtium*, *Rhubarb*, *Sunflowers* and *Marigold*. The flume was fed with 300 seeds during 4 min, and the flow was stopped after a total duration of 8 min. The number of seeds retained (i.e., permanently captured) was then counted visually (see Tab. 3.3).

Table 3.3: Number of captured seeds N_c (out of 300) and mean path length λ (m) between brackets, for the three different stem densities n_c (m^{-2}). The Corey Shape Factor (CSF), which measures the seed roundness, is also given as reported by *Chambert* [2006].

seed type	$n_c = 431\,m^2$	$n_c = 1251\,m^2$	$n_c = 1681\,m^2$	CSF
$sunflower$	20 (27.2)	44 (11.9)	51 (10.1)	0.43
$nasturtium$	194 (1.8)	20 (27.2)	215 (1.5)	0.19
$african\,daisy$	134 (3.2)	155 (2.6)	162 (2.4)	0.15
$rhubarb$	137 (3.1)	141 (3.0)	149 (2.7)	0.54
$nasturtium$	5 (111.9)	21 (25.9)	29 (25.9)	0.87

The mean path length given in Tab. 3.3 was calculated from Eq.3.3, specifically

$$\lambda = -\frac{L}{\ln(X > L)} \tag{3.23}$$

where we take L=1.88 m, and $P(X > L)$ is the percentage of non-captured seeds, i.e., $P(X > L) = 1 - N_c/300$. Please note that the estimation of λ is rather uncertain, because it uses data for only a single value of L, rather than a large set of data (P, L) to fit $P(X > L)$, as in the present experiments. In addition, the experimental procedure adopted by *Chambert and James* is different from the present experiments. We follow the trajectory and fate of one particle at a time, whereas *Chambert and James* release all the 300 seeds in 4 minutes, allowing the seeds to accumulate within the array. As a result, when the number of captured seeds is large, seeds released near the end of the run find little or no room to interact with the cylinders, and may instead attach, to previously captured seeds (see, e.g., their Figure 14), forming clusters of seeds within the array. The clustering likely increases the probability of capture for seeds released later in the run, a behavior that is not included in the present model. As a consequence the mean path length λ of the lighter seeds (i.e., *African Daisy*, *Marigold*, and *Rhubarb*), which are more easily trapped and thus exhibited more clustering, does not follow $1/n_c$, as observed in the present study. However, the heavier seeds, *Nasturtium* and *Sunflower*, which did not form clusters, exhibit the relationship $\lambda \sim n^{-1}$ (Fig. 3.8), consistent with the model developed in this thesis. We use data for *Nasturtium* and *Sunflowers* seeds to compute P_c as it varies with U/U_e. We assume a contact angle α in the range 15°-35° for *Sunflowers seeds*, whereas for *Nasturtium* seeds we measured a contact angle α=17.5°. In both cases we assume, for the cylinder, a contact angle α_c=55° (i.e. the same contact angle for the cylinders used in the present experiments). We then compute the meniscus slope angle at the particle

contact line ψ_p (see Tab. 3.4), the escape velocity U_e and the interaction efficiency P_i (see Tab. 3.5).

Table 3.4: Summary of seeds characteristics. The average diameter is computed as the geometric average of the three orthogonal long d_1, intermediate d_2 and short axes d_3. The seed density is computed as the ratio of seed mass to the volume of a sphere having the average diameter. Diameters d_1, d_2, and d_3 and seed mass are given by *Chambert* [2006].

seed type	*average diam.* (mm)	*mass* $(g/seed)$	ρ_p/ρ	$n_c d_c \lambda$	α $(^\circ)$	ψ_p $(^\circ)$
$sunflower$	6.2	0.0576	0.46	77.44	$15-35$	$21.0-29.5$
$nasturtium$	7.0	0.1320	0.73	227.32	$12-19$	$18.8-23.5$
$rhubarb$	4.7	0.0169	0.32	7.97 22.22 27.62	$38-46$	$14.7-16.9$

Combining Eqs. 3.8 with 3.5 we have

$$\ln(1-P_c) = -\frac{1}{P_i d_c n_c \lambda} \tag{3.24}$$

We use d_c=0.006 m and the mean experimental value for $n_c\lambda$ ($n_c\lambda \approx 3.5{\cdot}10^4$ m^{-1} for *Nasturtium* seeds and $n_c\lambda \approx 1.5{\cdot}10^4$ m^{-1} for *Sunflowers* seeds) in the above equation to compute the probability of capture P_c (see Tab. 3.4). The points are plotted in Fig. 3.9, and they compare favorably with the theoretical curve. It is interesting to observe in Tab. 3.5 that the capture probability is not very sensitive to contact angle α so that uncertainties in evaluating α have a minor impact on the estimation of P_c.

Finally, we also compute the capture probability for *Rhubarb* seed which, among the three lighter seeds, has the greatest roundness (CSF).We could not use *marigold* or *african daisy* because *i*) equation D.8 applies to spherical

Table 3.5: Summary of seeds computed model parameters.

seed type	$U_e\,(m/s)$	P_i	P_c
sunflower	$0.035 - 0.032$	$1.11 - 1.15$	$0.011 - 0.012$
nasturtium	$0.021 - 0.022$	$0.98 - 1.00$	$0.004 - 0.005$
rhubarb	≈ 0.039	$1.19 - 1.21$	$0.099 - 0.100$ ≈ 0.037 ≈ 0.030

particles (and extending equations in the Appendix D to different shapes is not straightforward) and *ii*) given the small thickness of these seeds it is very difficult to measure their contact angle. Since the product $n_c\lambda$ is not constant in this case, we compute three different values for P_c using the mean path lengths λ given in Tab. 3.3 for the three different cylinder densities. Results are plotted in Fig. 3.9 and again a good agreement with the theory is found.

Conclusions

In this work we studied the dynamics of floating particles in presence of emergent vegetation.

Preliminary experimental investigations allowed us to recognize the main particle-plant interaction mechanisms, i.e.: *i*) inertial impaction, *ii*) wake trapping, *iii*) capture due to surface tension (i.e. the Cheerios effect) and *iv*) net trapping.

A stochastic model based on these observations was proposed in order to describe the particle-plant interaction. In particular the proposed model describes the effects of the two most effective mechanisms listed above, i.e.: *i*) a permanent capture of particle due to the Cheerios effect and the net trapping, *ii*) a temporary trapping for a long retention time due to retention by the leaves through the Cheerios effect or by weak net trapping, and *iii*) a temporary trapping for a short retention time mainly due to the mechanisms of inertial impaction and wake trapping.

Further experimental investigations were carried out using plastic plants which resemble *spartina maritima* to improve and validate the model. Specifically, we focused on the effects of canopy density and flow velocity on the parameters of the model. The observations also allowed us to select the correct length scale of the problem Δs and to recognize the existence of two dramatically different retention times scales.

Although it would be desirable to add more experimental investigation in order to have an exhaustive picture of the issue, the proposed model

represents the first attempt to model the problem and it is an important tool perform *a priori* quantitative analysis of particle diffusion.

In the last part of the work we studied the influence of the Cheerios effect on the particle trapping by both numerical analysis and experimental investigation. In order to enhance our knowledge on the importance of the Cheerios effect an array of rigid dowels were adopted to mimic vegetation, so that the capture due to net trapping vanished. Through an extensive series of numerical simulations we could reconstruct and analyses particle trajectories and the capture modes of a cylindrical collector were described. The experimental investigation using rigid dowels allowed us to improve the stochastic model. In this condition the probability of interaction, P_i, and the probability of capture, P_c, can be written as function of bulk flow velocity and particle and cylinder characteristics. We also found that the proposed improvements have a general validity and it can be extended to described the capture due to the Cheerios effect by the leaves of complex plants.

Future development could focus in depth analysis of the net trapping mechanisms.

Moreover, it would be interesting to study how particles move in the presence of patches of vegetation and the effects of the particle clustering, since data found in the literature show that, in the presence of clusters, the mean distance travelled by particles is not related to the inverse of plants density anymore.

Far as numerical analysis is concerned, the study of the Cheerios effect in flow should be extended to an array of cylinders in the transition and turbulent regimes (i.e., Re¿10) to observe how wakes flow and the presence of more cylinder close each other could affect the ability of capture of cylindrical collector.

References

ALLDREDGE, A.L. and C. GHTSCHALK (1988), In situ settling behavior of marine snow. *Limnol. Oceanogr.*, 33, 339-351.

ANDERSSON, E., C. NILSSON, and M. E. JOHANSSON (2000), Plant dispersal in boreal rivers and its relation to the diversity of riparian flora. *J. Biogeogr.*, 27, 1095-1106.

BARTON, I.E. (1995), Computation of particle tracks over a backward-facing step. *J. Aerosol Sci.*, 26, 887-901.

BOUMA, T.J., M. FRIEDRICHS, B.K. van WESENBEECK, S. TEMMERMAN, G. GRAF and P.M.J. HERMAN (2009), Density-dependent linkage of scale-dependent feedbacks: a flume study on the intertidal macrophyte Spartina anglica. *Oikos*, 118, 260-268.

BRANDON, D.J. and S.K. AGGARWAL (2001), A Numerical Investigation of Particle Deposition on a Square Cylinder Placed in a Channel Flow. *Aerosol Sci. Tech.*, 34, 340-352.

BUSH, J.W.M., D.L., HU and M. PRAKASH, The Integument of Water-walking Arthropods: Form and Function. *Adv. In Insect. Phys.*, 34, 117-192.

BUTMAN, C.A. (1986), Larval settlement of soft-sediment invertebrates: some predictions based on an analysis of near-bottom velocity profiles. *Marine Interfaces Ecohydrodynamics*, 487-513.

CALLAGHAN, D.P., T.J. BOUMA, P. KLAASSEN, D. van der WAL, M.J.F. STIVE and P.M.J. HERMAN (2010), Hydrodynamic forcing on salt-marsh development: Distinguishing the relative importance of waves and tidal flows. Estuarine. *Coastal and Shelf Science*, 89, 73-88.

CHAMBERT, S. (2006), Sorting of Seeds by Hydrochory. *Master Thesis.*

CHAMBERT, S., and C. S. JAMES (2009), Sorting of seeds by hydrochory. *River Res. Appl.*, 25, 48-61.

CHANG, E.R., R.M. VEENEKLAAS, R. BUITENWERF, J.P. BAKKER and T.J. BOUMA (2008), To move or not to move: determinants of seed retention in a tidal marsh. *Functional Ecology*, 22, 260-268.

DUSHKIN, C.D., P.A. KRALCHEVSKY, V.N. PAUNOV, H. YOSHIMURA and K. NAGAYAMA (1996), Torsion Balance for measurement of capillary immersion forces. *Langmuir*, 12, 641-651.

FEY, U., M. KONING, and H. ECKELMANN (1998), A new Strouhal-Reynolds number relationship for the circular cylinder in the range 47 ¡ Re ¡2 105. *Phys. Fluids*, 10(7), 1547-1549.

GAYLORD B., D.C. REED, P.T. RAIMONDI, L. WASHBURN and S.R. McLEAN (2002), A physically based model of macroalgal spore dispersal in the wave and current-dominated nearshore. *Ecology*, 83(5), 1239-1251.

GIBBS, R.J. (1985), Estuarine Flocs: Their Size, Settling Velocity and Density. *J. Geophys. Res.*, 90, 3249-3251.

GROVES, J. H., D. G. WILLIAMS, P. CALEY, R. H. NORRIS, and G. CAITCHEON (2009), Modeling of floating seed dispersal in a fluvial environment. *River. Res. Applic.*, 25, 582-592.

HUISKES, A.H.L., B.P. KOUTSTALL, P.M.J. HERMAN, W.G. BEEFTINK, M. M. MARKUSSE, and W. De MUNCK (1995), Seed dispersal of halophyte in tidal salt marshes. *J. Ecol.*, 83, 559-567.

JACKSON, G.A. (1989), A model of the formation of marine algal flocs by physical coagulation processes. *Limnol. Oceanogr.*, 34, 514-530.

JIN K.R. and JI Z.G., 2005, Application and Validation of Three-Dimensional Model in a Shallow Lake. *Journal of Waterway, Port, Coastal, and Ocean Engineering*, sept.-oct., 213-225.

JOSEPH, D.D., J. WANG, R. BAI, B.H. YANG and H.H. HU (2001), Particle motion in a liquid film rimming the inside of a partially filled rotating cylinder. *J. Fluid Mech.*, 496, 139-163.

KRALCHEVSKY, P.A. and K. NAGAYAMA (2000), Capillary interactions between particles bound to interfaces, liquid films and biomembranes. *Advances in Colloid and Interface Science*, 85, 145-192.

KRALCHEVSKY, P.A. and N.D. DENKOV (2001), Capillary forces and structuring in layers of colloid particles. *Current Opinion in Colloid & Interface Science*, 6, 383-401.

LA BARBERA (1984), Feeding currents and particle capture mechanisms in suspension feeding animals. *Am. Zool.*, 24, 71-84

LI C.W. and K. YAN (2007), Numerical Investigation of Wave-Current-Vegetation Interaction. *Journal of Hydraulic Engineering*, 794-803.

LI C.W. and L.H. YU (2010), Hybrid LES/RANS modelling of free surface flow through vegetation. *Computers & Fluids*, 39, 1722-1732.

LI C.W. and M.L. ZHANG (2010), 3D modelling of hydrodynamics and mixing in a vegetation field under waves. *Computers & Fluids*, 39, 604-614.

LIGHTBODY, A.F., and H.M. NEPF (2006), Prediction of velocity profiles and longitudinal dispersion in emergent salt marsh vegetation. *Limnol. Oceanogr.*, 51(1), 218-228.

LOPEZ, F., and M. GARCIA (1998), Open-channel flow through simulated vegetation: Suspended sediment transport modeling. *Water Resour. Res.*, 34(9), 2341-2352.

MERRIT, D.M., and E.E. WOHL (2002), Processes governing hydrochory along rivers: Hydraulics, hydrology, and dispersal phenology. *Ecol. Appl.*, 12, 1071-1087.

MURPHY, E., M. GHISALBERTI, and H. NEPF (2007), Model and laboratory study of dispersion in flows with submerged vegetation, *Water Resour. Res.*, 43, W05438, doi:10.1029/2006WR005229.

NEPF, H.M. (1999) Drag, turbulence, and diffusion in flow through emergent vegetation. *Water Resour. Res.*, 35(2), 479-489.

NEPF, H., M. GHISALBERTI, B. WHITE, and E. MURPHY (2007), Retention time and dispersion associated with submerged aquatic canopies. *Water Resour. Res.*, 43, W04422, doi:10.1029/2006WR005362.

NILSSON, C., E. ANDERSSON, D.M. MERRIT and M.E. JOHANSSON (2002), Differences in riparian flora between riverbanks and river lakeshores explained by dispersal traits. *Ecology*, 83, 2878-2887.

NILSSON, C., and M. DANVIND (1997), Seed floating ability and distribution of alpine plants along a northern Swedish river. *J. Veg. Sci.*, 8, 271-276.

PATIL S., X. LI, C. LI, B.Y.F. TAM, C.Y. SONG, Y.P. CHEN and Q. ZHANG (2009), Longitudinal dispersion in wave-current-vegetation flow. *Physical Oceanography*, Vol. 19, No. 1.

PALMER, M.R., H.M. NEPF AND T.J.R PETTERSON (2004), Observations of particle capture on a cylindrical collector: Implications for particle accumulation and removal in aquatic systems. *Limnol. Oceanogr.*, 49, 1, 76-85.

RAND, T.A. (2000), Seed dispersal, habitat suitability and the distribution of halophytes across a salt marsh tidal gradient. *J. Ecol.*, 88, 608-621.

REISE K. (2002), Sediment mediated species interactions in coastal waters. *Journal of Sea Research*, 48, 127-141.

RIIS, T., and K. SAND-JENSEN (2006), Dispersal of plant fragments in small streams. *Freshwater Biol.*, 51, 274-286.

RUBESTEIN, D.I. and M.A.R. KOHEL (1997), The mechanisms of filter feeding: some theoretical considerations. *The American Naturalist*, 111 (981), 981-994.

SCHIMETA, J. and P.A. JURMAS (1991), Physical mechanisms and rates of particle capture by suspension feeders. *Oceanogr. Mar. Biol. Annu. Rev.*, 29, 191-257.

SILVESTER, N.R. and M.A. SLEIGH (1984), Hydrodynamic aspects of particle capture by Mytilus, *J. Mar. Biol. Assoc. U.K.*, 64 (4), 859-879

SHARPE, R.G., and C.S. JAMES (2006), Deposition of sediment from suspension in emergent vegetation. *Water SA*, 32(2), 211-218.

SULLIVAN P.P. and J.C. McWILLIAMS (2010), Dynamics of Winds and Currents Coupled to Surface Waves. *Annu. Rev. Fluid Mech.*, 42, 19-42.

TURNER S.J., J.E. HEWITT, M.R. WILKINSON, D.J. MORRISEY, S.E. THRUSH, V. J. GUMMINOS and G. FUNNEL (1999), Seagrass Patches and Landscapes: The Influence of Wind-wave Dynamics and Hierarchical Arrangements of Spatial Structure on Macrofaunal Seagrass Communities. *Estuaries*, Vol. 22, No. 4, p. 1016-1032.

UMEDA, S. and W.J. YANG (1991), Dynamics of particles floating on liquid flowing in a semicircular open channel. *Experiments in fluid*, 12, 106-112.

Van den BROEK, T., R. van DIGGELEN, and R. BOBBINK (2005), Variation in seed buoyancy of species in wetland ecosystems with different flooding dynamics. *J. Veg. Sci.*, 16(5), 579-586.

Van der HEIDE, T., E.H. van NES, G.W. GEERLING, A.J.P. SMOLDERS, T.J. BOUMA and M.M. van KATWIJK (2007), Positive Feedbacks in Seagrass Ecosystems: Implications for Success in Conservation and Restoration. *Ecosystems*, 10, 1311-1322.

VELLA, D. and L. MAHADEVEN (2005), The "Cheerios effect". *Am. J. Phys.*, 73, 9, 817-825.

WHITE, B.L. and H.M. NEPF (2003), Scalar transport in random cylinder arrays at moderate Reynolds number. *J. Fluid Mech.*, 487, 43-79.

WHITE, F.M. (1991), *Viscous fluid flow*, Second Edition. McGraw-Hill, Inc.

WOLTERS, M., A. GARBUTT, R.M. BEKKER, J. P. BAKKER, and P.D. CAREY (2008), Restoration of salt-marsh vegetation in relation to site suitability, species pool and dispersal traits. *J. Appl. Ecol.*, 45, 904-912.

Appendix A

Analytical expression for the arrival time distribution function

We focus on particles that actually travel the distance $X \geq L$ (i.e., particles that are permanently captured over a path shorter than L are a priori excluded from the present analysis), and we assume that the number of interaction points, $n = L/\Delta s$ within the distance L is an integer.

The probability $p(k)$ that a particle interacts k (out of n) times with the vegetation has a binomial distribution with mean nP_i and variance $nP_i(1 - P_i)$

$$p(k) = \frac{n!}{k!(n-k)!} P_i^k (1 - P_i)^{n-k}, \tag{A.1}$$

P_i being the probability that, at each interaction point, the particle actually interacts with the vegetation.

When a particle interacts with one leaf it can be either slowed down (i.e., trapped for a short time, see Fig. 1.9) or trapped for a long time (as stated above, permanent trapping is not considered here).

Let m ($\leq k$) be the number of short time trapping events. The probability of having m out of k short time interactions follows a binomial distribution

$$q(m) = \frac{k!}{m!(k-m)!} P_S^m (1 - P_S)^{k-m} \tag{A.2}$$

where P_S is the probability that the interaction event is actually a short-time interaction.

The retention time distribution $r_{m,k}(t)$, for a particle that experiences m short retention time trapping events out of k (temporarily) trapping events is then given as

$$r_{m,k}(t) = \underbrace{p_S * p_S * .... * p_S}_{m\ times} * \underbrace{p_L * ..... * p_L}_{k-m\ times} \tag{A.3}$$

where $*$ denotes convolution, and

$$p_S(t) = \frac{1}{T_S} e^{-t/T_S} \quad , \quad p_L(t) = \frac{1}{T_L} e^{-t/T_L} \tag{A.4}$$

are the short and long retention time distributions, here assumed to be exponential with means T_S and T_L, respectively.

The retention time distribution is then given as

$$r(t) = \sum_{k=0}^{n} \left[p(k) \sum_{m=0}^{k} q(m)\, r_{m,k}(t) \right] \tag{A.5}$$

Equation (A.5) gives the time a particle spends at rest (in the sense of the proposed model, see Fig. 1.9). To determine the total time a particle spends within the reach L we must add the particle travel time which is affected by the turbulent diffusion mainly due to the spatially non-uniform velocity field. Assuming a Fickian diffusion, the travel time distribution $h(t)$ is then given as

$$h(t) = \frac{L}{4\sqrt{\pi D t^3}} e^{-\frac{(L-U_0 t)^2}{4Dt}} \tag{A.6}$$

where D is the diffusion coefficient.

The arrival time distribution function $a(L,t)$ is then given as the convolution of equations (A.5) and (A.6)

$$a(L,t) = \sum_{k=0}^{n} \left[p(k) \sum_{m=0}^{k} q(m)\ (r_{m,k}(t) * h(t)) \right] \tag{A.7}$$

If we neglect diffusion, then $h(t)$ reduces to the Dirac Delta function $\delta(t - t_0)$, with $t_0 = L/U_0$, and Eq. (A.7) can be rewritten as

$$a(L,t) = \begin{cases} 0 & t \le t_0 \\ \sum_{k=0}^{n} \left[p(k) \sum_{m=0}^{k} q(m)\, r_{m,k}(t - t_0) \right] & t > t_0 \end{cases} \tag{A.8}$$

where $p(k)$ and $q(m)$ are given by equations (A.1), (A.2) respectively, and the retention time distribution $r_{m,k}(t)$ can be developed as follows.

By combining equations (A.3) and (A.4), we find that $r_{m,k}(t)$ is given as the convolution between two Gamma distributions associated with the short and the long retention times respectively

$$r_{m,k}(t) = \left[\frac{t^{m-1}e^{-t/T_S}}{T_S^m(m-1)!}\right] * \left[\frac{t^{k-m-1}e^{-t/T_L}}{T_L^{k-m}(k-m-1)!}\right] \tag{A.9}$$

Equation (A.9) is expanded to read

$$\begin{aligned} r_{m,k}(t) &= \frac{e^{-t/T_L}}{T_S^m T_L^{k-m}(m-1)!(k-m-1)!} \cdot \\ &\quad \cdot \int_0^t e^{\Psi\tau}\tau^{m-1}(t-\tau)^{k-m-1}d\tau \end{aligned} \tag{A.10}$$

where $\Psi = 1/T_L - 1/T_S$. Eq. (A.10) is then recast as

$$\begin{aligned} r_{m,k}(t) &= \frac{e^{-t/T_L}t^{k-1}}{T_S^m T_L^{k-m}(m-1)!(k-m-1)!} \cdot \\ &\quad \cdot \int_0^1 e^{\Psi t\xi}\xi^{m-1}(1-\xi)^{k-m-1}d\xi \end{aligned} \tag{A.11}$$

Recalling that

$$(1-\xi)^n = \sum_{i=0}^{n} \frac{n!}{(n-i)!\,i!}(-\xi)^i, \tag{A.12}$$

the integral in Eq. (A.11) can be written as

$$\begin{aligned} &\int_0^1 e^{\Psi t\xi}\xi^{m-1}(1-\xi)^{k-m-1}d\xi = \\ &= \sum_{i=0}^{k-m-1} \frac{(k-m-1)!}{(k-m-i-1)!\,i!}(-\xi)^i \int_0^1 e^{\Psi t\xi}\xi^{i+m-1}d\xi \end{aligned} \tag{A.13}$$

Finally, using the following recursive formula

$$\int_0^1 e^{\Psi t\xi}\xi^n d\xi = \frac{e^{\Psi t}}{\Psi t} - \frac{n+1}{\Psi t}\int_0^1 e^{\Psi t\xi}\xi^{n-1}d\xi, \tag{A.14}$$

Eq. (A.11) is rewritten as

$$\begin{aligned} r_{m,k}(t) &= \frac{e^{-t/T_L}t^{k-1}}{T_S^m T_L^{k-m}(m-1)!} \cdot \sum_{i=0}^{k-m-1} \frac{(i+m-1)!}{(k-m-i-1)!\,i!} \cdot \\ &\cdot \left[\frac{(-1)^m}{(\Psi t)^{i+m}} + \frac{e^{\Psi t}}{\Psi t}\sum_{j=0}^{i-m-1}\frac{(-1)^{i+j}}{(\Psi t)^j(i+m-j-1)!}\right] \end{aligned} \tag{A.15}$$

If the ratio $L/\Delta s$ is not an integer, we have $L_0 < L < L_1$, with $L_0 = n\Delta s$ and $L_1 = (n+1)\Delta s$. Because the interaction points are assumed uniformly distributed, then the arrival time distribution is given as the following weighted average

$$a(L,t) = w \cdot a(L_0,t) + (1-w)\cdot a(L_1,t) \tag{A.16}$$

with $w = (L_1 - L)/\Delta s$.

Appendix B

The random walk particle-tracking model

The random walk particle-tracking model developed to predict floating particle paths in the presence of emergent vegetation is based on the scheme shown in Fig. 1.9. The Lagrangian trajectory of each single particle is computed using the following steps.

As a first step, the model generates a series of interaction points, randomly distributed with a uniform *pdf* and one point within each segment Δs. The model then computes the particle path advancing in time by small time steps $\Delta t = 0.001$ s.

At each time step the model checks if the particle has reached an interaction point. If this is not the case, the particle is advanced with velocity $U_0 + \Delta U$, ΔU being a (random) velocity fluctuation which accounts for turbulent diffusion. This velocity fluctuation is randomly generated from a Gaussian distribution with zero mean and standard deviation $\sigma_U = \sqrt{2D/\Delta t}$, D being the turbulent diffusion coefficient.

When the particle reaches an interaction point a random number r is generated (with $0 \leq r \leq 1$, and a uniform *pdf*): if $r > P_i$ then the model assumes that the particle dos not interact with the vegetation and it is advanced one time step as described above.

Otherwise ($r \leq P_i$), the particle is assumed to interact with the vegetation. In this case a further random number r is generated, and if $r \leq P_c$ then the model assumes that the particle is permanently captured by the vegetation and the path reconstruction ends.

If the particle is temporarily captured (i.e., $r > P_c$) a further random number r is generated to establish whether the temporary capture is a short-time or a long-time trapping event. If $r \leq P_L$ the model assumes the interaction to be a long-time trapping event; a random retention time t_R, exponentially distributed with mean T_L, is then generated

and the particle is left in place for this period of time. On the contrary (i.e., if $r > P_L$) the model assumes the interaction to be a short-time interaction event; in this case a random retention time t_R, exponentially distributed with mean T_S, is generated and the particle is left in place for this period of time.

The path reconstruction keeps going until the particle is permanently captured or until the particle has travelled a distance greater than or equal to the test section length. For each reconstructed path (realization) the model then gives the particle position at each time $t_i = i\Delta t$.

Appendix C

Model parameters estimation

The procedure adopted to estimate the number of lacking data N_0 in Eq. 2.4 and to assess model parameters P_L, T_S, T_L is here detailed. To this aim we use measured retention times t_i, which are sorted in increasing order to form a set of pairs (i, t_i), i=1 to N_i.

As a preliminary step, we compute a first guess for N_0 using a subset of pairs (i, t_i) containing only the shortest retention times t_i (t_i <0.8 s). Combining Eqs. 2.3 and 2.4 we obtain

$$\frac{N_i + 1 - i}{N_i + N_0 + 1} = P_L e^{-t_i/T_L} + (1 - P_L) e^{-t_i/T_S} \tag{C.1}$$

The exponential functions in the above equation are approximated with a first-order Taylor expansion about t=0; moreover, since T_L is much greater than T_S, we neglect t_i/T_L compared to t_i/T_S and write

$$\frac{N_i + 1 - i}{N_i + N_0 + 1} \approx 1 - \frac{t_i}{T_S}(1 - P_L) \tag{C.2}$$

which is rearranged to read

$$i \approx \left[(1 - P_L)\frac{N_i + N_0 + 1}{T_S}\right] t_i - N_0 \tag{C.3}$$

N_0 is then given as the intercept of the above straight line (linear regression).

The second step then finds a first approximation for T_L. We use a subset of pairs (i, t_i) containing only the longest retention times (t_i >10 s). Note that, since T_S is expected to be of the order of $1 \sim 2$ s then $\exp(-t/T_S)$ turns out to be negligibly small when t >10 s. We then write

$$\frac{N_i + 1 - i}{N_i + N_0 + 1} \approx P_L e^{-t_i/T_L} \tag{C.4}$$

We fit experimental data to the above equation and find T_L and P_L.

The last step considers the full set of data. Equation C.1 is rewritten as

$$\frac{1}{1-P_L}\left[\frac{N_i+1-i}{N_i+N_0+1}-P_L e^{-t_i/T_L}\right]=e^{-t_i/T_S} \tag{C.5}$$

and T_S is computed as

$$T_S=-\frac{1}{N_i}\sum_{i=1}^{N_i}\frac{t_i}{\ln\left\{\frac{1}{1-P_L}\left[\frac{N_i+1-i}{N_i+N_0+1}-P_L e^{-t_i/T_L}\right]\right\}} \tag{C.6}$$

We then compute the determination coefficient R^2 using the full set of data and use a trial and error approach to fine tune model parameter in order to maximize R^2.

Appendix D

Vertical equilibrium of lighter than water hydrophilic sphere in water

The meniscus slope angle at the particle contact line ψ_i is estimated by the dynamic analysis of vertical force acting on a floating sphere (see Fig. D.1).

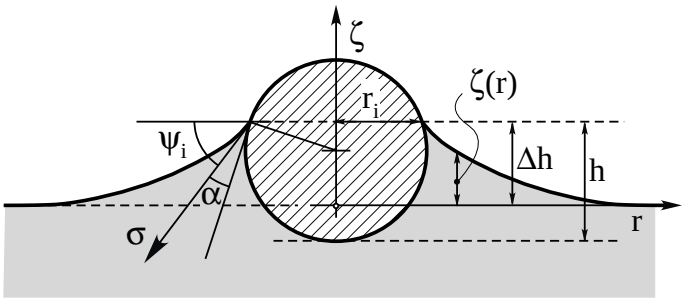

Figure D.1: Forces acting on floating particle with density $\rho_p < \rho$; σ is the surface tension acting along the wetted perimeter. adapted from [*Kralchevsky and Nagayama*, 2000].

For light particle ($\rho_p < \rho$) the equilibrium position is reached when the forces due to the weight of the sphere and the surface tension in vertical direction are equal to pressure force acting on the sphere:

$$\frac{\pi d_p^3}{6}\rho_p g + 2\pi r_i \sigma \sin(\psi_i) = \pi h^2 \left(\frac{d_p}{2} - \frac{h}{3}\right)\rho g - \rho g \Delta h \pi r_i^2 \tag{D.1}$$

here the first term is the sphere weight and the second term is the force due to the surface tension. As far as concerned the pressure the first term on the right hand side of Eq. D.1 is in agreement with Archimedes' principle while the last term accounts for the meniscus effect. Because of elementary geometric consideration the contact radius is $r_i = \frac{d_p}{2}\sin(\alpha + \psi_i)$ and Eq. D.1 can be rewritten as

$$\frac{\pi d_p^3}{6}\rho_p g + \pi\sigma \sin(\psi_i)\sin(\alpha + \psi_i) = \pi h^2 \left(\frac{d_p}{2} - \frac{h}{3}\right)\rho g - \rho g \frac{\pi d_p^2}{4}\Delta h \sin^2(\alpha + \psi_i) \tag{D.2}$$

The contact radius r_i can also be written as:

$$r_i = \sqrt{\frac{d_p^2}{4} - \left(\frac{d_p}{2} - h\right)^2} \tag{D.3}$$

Through Eq. D.3 and the previous definition of r_i the sphere immersion h can be function of the meniscus slope angle ψ_i:

$$h = \frac{d_p}{2}\left[1 + \sqrt{1 - \sin^2(\alpha + \psi_i)}\right] = \frac{d_p}{2}\left[1 + \cos(\alpha + \psi_i)\right] \tag{D.4}$$

Replacing Eq. D.4 in Eq. eqD2 and rearranging the equation, the equilibrium position of the sphere is finally given by:

$$\sin(\alpha + \psi_i)\sin(\psi_i) + Bo\left[\frac{\rho_r}{6} - \frac{2 + 3\cos(\alpha + \psi_i) - \cos^3(\alpha + \psi_i)}{24} + \right.$$
$$\left. + \frac{\sin^2(\alpha + \psi_i)\Delta h}{4 d_p}\right] = 0 \tag{D.5}$$

where ρ_r is the relative sphere density and $Bo = \frac{\rho g d_p^2}{\sigma}$ is the Bond number that represents the ratio between gravitational force and surface tension.

Some studies describe analytically $\zeta = \zeta(r)$ (see Fig. D.1. According to *Kralchevsky and Nagayama* (2000) we can write the shape that meniscus formed around the sphere as:

$$\zeta(r) = r_i \sin(\psi_i) K_0(r/l_c) \tag{D.6}$$

here l_c is the capillary length.

By considering the contact radius r_i as $d_p/2sin(\alpha + \psi_i)$ in Eq. D.6, the rise of the meniscus in comparison to the undisturbed free surface is at contact to the sphere:

$$\Delta h = \frac{d_p}{2}\sin(\alpha + \psi_i)\sin(\psi_i) K_0\left(\frac{d_p}{2l_c}\sin(\alpha + \psi_i)\right) \tag{D.7}$$

By replacing Eq. D.7 in Eq. D.5 the equilibrium equation becomes:

$$\sin(\alpha+\psi_i)\sin(\psi_i) + Bo\left[\frac{\rho_r}{6} - \frac{2+3\cos(\alpha+\psi_i)-\cos^3(\alpha+\psi_i)}{24} + \right.$$
$$\left. + \frac{\sin^3(\alpha+\psi_i)\sin(\psi_i)K_0\left(\frac{d_p}{2l_c}\sin(\alpha+\psi_i)\right)}{8}\right] = 0 \qquad \text{(D.8)}$$

In Eq. D.8 Bo, α and ρ_r are known by the physics and geometric characteristics of the particle and the meniscus slope angle ψ_i is the unknown quantity of the problem.

Appendix E

Numerical solution of the floating particle dynamics equation

The numerical solution of the particle trajectories in Section 3.1 is given as the solution to equation:

$$\left(\frac{\rho_r+\beta}{\rho_r}\right)\frac{d\mathbf{u_p}}{dt}=\frac{3\pi C_d}{4\rho_r L_p}\mathbf{U}\left|\mathbf{U}\right|-\frac{3\sigma d_c}{\rho_p l_c d_p^2}\sin(\alpha+\psi_p)\sin(\psi_p)\sin(\psi_c)K_1(\mathbf{r}/l_c) \tag{E.1}$$

The variables in Eq. E.1 are the same of Eqs. 3.1 and Eqs. 3.1. By averaging over the timestep Δt, Eq. 1.1 can be rewritten as:

$$\begin{aligned}\left(\frac{\rho_r+\beta}{\rho_r}\right)\frac{1}{\Delta t}\int_t^{t+\Delta t}\frac{d\mathbf{u_p}}{dt}dt=\frac{3\pi C_d}{4\rho_r L_p}\frac{1}{\Delta t}\int_t^{t+\Delta t}\mathbf{U}\left|\mathbf{U}\right|dt+\\ -\frac{1}{\Delta t}\int_t^{t+\Delta t}\frac{3\sigma d_c}{\rho_p l_c d_p^2}\sin(\alpha+\psi_p)\sin(\psi_p)\sin(\psi_c)K_1(\mathbf{r}/l_c)dt\end{aligned} \tag{E.2}$$

By expanding Eq. E.2 we find:

$$\begin{aligned}\left(\frac{\rho_r+\beta}{\rho_r}\right)\frac{\mathbf{u_p}(t+\Delta t)-\mathbf{u_p}(t)}{\Delta t}=\frac{3\pi C_d}{4\rho_r L_p}\left[\mathbf{U}(t+\Delta t)\cdot\left|\mathbf{U}(t)\right|\right]+\\ -\left(\frac{3\sigma d_c}{\rho_p l_c d_p^2}\sin(\alpha+\psi_p)\sin(\psi_p)\sin(\psi_c)K_1(r/l_c)\right)_t\end{aligned} \tag{E.3}$$

In Eq. E.3 the first term on the right hand side is the geometric mean of the respective term in Eq. E.2 and the rightmost term is written at time t.

By replacing $\mathbf{U} = \mathbf{u_f} - \mathbf{u_p}$ Eq. E.3 is rewritten as:

$$\left(\frac{\rho_r + \beta}{\rho_r}\right) \frac{\mathbf{u_p}(t + \Delta t) - \mathbf{u_p}(t)}{\Delta t} = \frac{3\pi C_d}{4\rho_r L_p}\Bigg[(\mathbf{u_f}(t + \Delta t) - \mathbf{u_p}(t + \Delta t)) \cdot \cdot |\mathbf{U}(t)|\Bigg] - \left(\frac{3\sigma d_c}{\rho_p l_c d_p^2} \sin(\alpha + \psi_p) \sin(\psi_p) \sin(\psi_c) K_1(r/l_c)\right)_t \tag{E.4}$$

Finally eq. E.4 is recast as:

$$\mathbf{u_p}(t + \Delta t) = \frac{1}{\left[\left(\frac{\rho_r+\beta}{\rho_r}\right) \frac{1}{\Delta t} + \frac{3\pi C_d}{4\rho_r L_p} |\mathbf{U}(t)|\right]}\Bigg[\left(\frac{\rho_r + \beta}{\rho_r}\right) \frac{\mathbf{u_p}(t)}{\Delta t} + \frac{3\pi C_d}{4\rho_r Lp} \cdot \cdot |\mathbf{U}(t)| \, \mathbf{u_f}(t + \Delta t) - \left(\frac{3\sigma d_c}{\rho_p l_c d_p^2} \sin(\alpha + \psi_p) \sin(\psi_p) \sin(\psi_c) K_1(r/l_c)\right)_t\Bigg] \tag{E.5}$$